UCLouvain

École polytechnique de Louvain

Investigation of dynamic stall in actuator line and surface models for VAWTs

Author: **Bastien Adriaens**
Supervisors: **Philippe Chatelain, Matthieu Duponcheel**
Readers: **Vincent Legat, Johan Meyers, Maud Moens**
Academic year 2019–2020
Master [120] in Mechanical Engineering

Abstract

This work aims to better model the aerodynamic behaviour of vertical axis wind turbines or VAWTs by focusing on the complex phenomenon of dynamic stall, which arises when a blade recurrently and quickly undergoes large changes of angle of attack. This analysis is done in the frames of an actuator line and an actuator cylinder model coupled with a Large Eddy Simulation code and validated in view of a high fidelity vortex-particle mesh method.

The results reveal that actuator line and cylinder models provide good agreement between each other in terms of forces even if some small differences logically appear in the velocity fields. Taking the model of dynamic stall into account by far increases the power for low TSRs. A more refined dynamic stall model is then implemented and proves to increase the power of the VAWT. At last, the VAWTs are simulated with an actuator line model and an actuator cylinder model with the dynamic stall and a turbulent inflow. The latter allow both models to get closer.

Acknowledgements

My first thank goes to my supervisors, Professors Philippe Chatelain and Matthieu Duponcheel, for their advised guidelines and expertise through this thesis.

I would also like to deeply thank Doctor Maud Moens and Doctoral researcher François Trigaux for their support through this year. Their advices, technical help and availability were essential for the realisation of this work. My thanks also go to Denis-Gabriel Caprace and Gauthier Georis for their time and their expertise on the dynamic stall.

Moreover, I would like to thank Professors Johan Meyers and Vincent Legat to be part of my jury.

Then, I want to thank Magali for her support and her English corrections.

At last, computational resources have been provided by the supercomputing facilities of the Université catholique de Louvain (CISM/UCL) and the Consortium des Équipements de Calcul Intensif en Fédération Wallonie Bruxelles (CÉCI) funded by the Fond de la Recherche Scientifique de Belgique (F.R.S.-FNRS) under convention 2.5020.11 and by the Walloon Region.

Contents

List of Figures

List of Tables

List of Acronyms

AOA	Angle Of Attack
ACM	Actuator Cylinder Model
ALM	Actuator Line Model
AR	Aspect Ratio
CCGT	Combined Cycle Gas Turbine
DMST	Double Multiple Stream Tube
DNS	Direct Numerical Simulation
DS	Dynamic Stall
HAWT	Horizontal Axis Wind Turbine
LB	Leishman-Beddoes
LCOE	Levelized Cost Of Electricity
LES	Large Eddy Simulation
RANS	Reynolds-Averaged Navier-Stokes Simulation
SST	Single Stream Tube
TSR	Tip Speed Ratio
VAWT	Vertical Axis Wind Turbine
VPM	Vortex Particle Mesh
TI	Turbulent Intensity
TKE	Turbulent Kinetic Energy

Chapter 1

Introduction

1.1 Wind Power

In a world where the consumption of resources as well as the greenhouse gases emissions are increasing, striving to develop renewable energies has become a necessity. After hydropower, wind energy is the second most used renewable energy in the world today: it generated 840 TWh worldwide in 2015 and is expected to produce between 1897 and 3236 TWh in 2030 [40].

In order to provide an insight on the influence of wind energy in Belgium, the energy mixes for 2017 and 2018 are shown on figure 1.1 [14]. By summing offshore and onshore wind, it results that between 6.3 and 8% of the electricity in Belgium was provided by wind energy in 2018, which corresponds to a rise of approximately 1% compared to 2017. Another interesting number to illustrate the growing influence of the renewable energies is the following one : at some points in 2018, 46% of the electricity consumption in Belgium was covered by wind and solar energies [14].

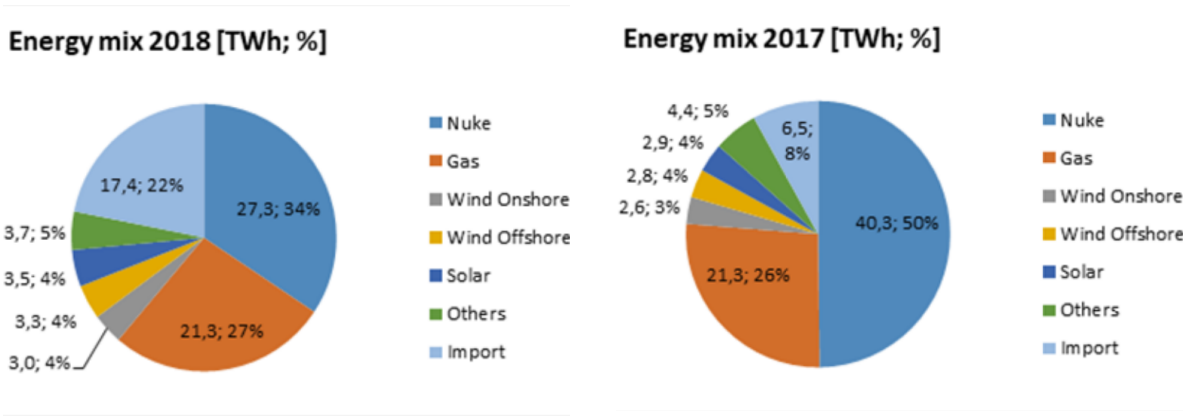

Figure 1.1: Energy mix in Belgium in 2017 and 2018 [14]

Wind energy has several advantages: it does not cause greenhouse gas emissions, is widely available and can offer a limited levelized cost of electricity (LCOE). This LCOE is defined as the overal cost of a wind turbine for example divided by its lifetime. This indicator takes into account the fixed and variable costs, from the initial investments

to the operation and maintenance costs, as well as the capacity factor [1]. In Germany, depending on the location, the LCOE of onshore wind power can reach 3.99€/kWh while no CCGT power plant has a LCOE lower than 7.78€/kWh [15]. However, it should be noted that a wind farm located at a less favourable place will have a higher LCOE in the same way that offshore wind power has a higher LCOE [15].

1.2 Vertical axis wind turbine

Whereas the most widely used type of wind turbine is the Horizontal Axis Wind Turbine (HAWT), many other configurations exist. Among others, the Vertical Axis Wind Turbine (VAWT), has many advantages compared to the HAWT and is worth studying. Indeed, conversely to the HAWTs, the VAWTs are independent of the flow direction and can produce energy without any yawing system, they are able to withstand high-turbulence winds, they enjoy easier maintenance due to their generator placed on the ground and they produce comparatively less noise [27]. Furthermore, thanks to the fact that the blades of a VAWT intersect two times with the flow, the limit of Betz of 59.3% for a HAWT which represents the maximal kinetic energy that could be extracted from the wind could be increased to 64% in a VAWT[6]. At last, the VAWTs exhibit a relatively faster wake recovery than the HAWTs, which can be interesting in the case of a wind farm [1]. However, despite all these advantages, way more research has been performed on HAWT than on VAWT and research on this kind of wind turbine has only been tackled in the past few years [7].

The aerodynamics of a VAWT is much more complex than the one of a HAWT, which is mainly due to the interactions between the blades and the wake and to the dynamic stall, the recurrent separation of the boundary layer on the blades as a result of the high-frequency varying angles of attack. This aerodynamic complexity is one of the reasons why the HAWTs are nowadays much more widespread than the VAWTs : as it is essential to dispose of a solid numerical model in order to dimension and compute a wind turbine before it is produced, it is commercially more attractive to opt for HAWTs [6]. Therefore, numerical research to strengthen the understanding of VAWTs is led and different models already exist to this end (see 1.3).

The vertical axis wind turbines can be divided into two main groups : the Savonius type and the Darrieus type. The drag force generates the power in the Savonius ones whereas the lift force generates the power in the Darrieus ones. Looking more closely at the Darrieus type, these wind turbines can be subdivided in 3 groups : the ϕ-rotor or parabolic, the helical rotor and the H-rotor [9]. This non-exhaustive classification of wind turbines can be seen more clearly on figure 1.2 where the drawings are coming from [33]. The ϕ-rotor is designed to limit the bending moment due to centrifugal effect [10]. Thanks to a better distribution of torque, the helical rotor exhibits a better behaviour concerning fatigue constraints -which can be substantial in VAWT- and provides a more constant torque during a revolution but requires higher production costs [33]. At last, the H-rotor or straight-blades rotor has the advantage to be easy to manufacture and

[1] This last one is generally comprised between 20% and 40% for a wind turbine [37].

to make comparatively less noise [37]. In this work, all the attention will be carried on the three-bladed Darrieus H-rotor VAWT.

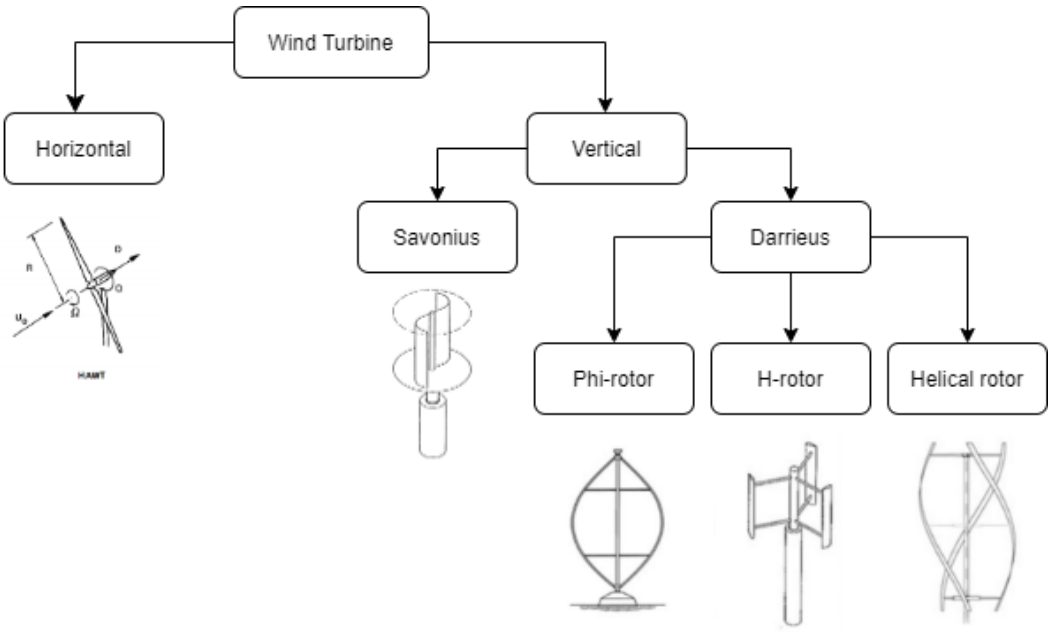

Figure 1.2: Non-exhaustive classification of wind turbines

At last, some classical and important parameters relative to the VAWTs have to be defined :

- The TSR for Tip Speed Ratio expresses the ratio between the speed at the blade tips ωR and the upstream wind speed U_∞.

$$TSR = \frac{\omega R}{U_\infty} \qquad [-] \tag{1.1}$$

  The TSR is sometimes also expressed with the Greek letter λ.

- The aspect ratio AR is defined as the ratio between the rotor height H and the diameter of the VAWT D.

$$AR = \frac{H}{D} \qquad [-] \tag{1.2}$$

- The solidity σ is the ratio between the surface of the blades divided by the swept area.

$$\sigma = \frac{Bc}{2R} \qquad [-] \tag{1.3}$$

  where B is the number of blades and c is the profile chord length of the blades. Different expressions exist to define the solidity and this one has been chosen to be consistent with previous works [9].

- The reduced frequency k is defined as the ratio between the product of the rotational speed of the VAWT by the chord of the blade and two times the free stream velocity. This parameter characterises the unsteadiness.

$$k = \frac{\omega c}{2U_\infty} \tag{1.4}$$

1.3 Simulation methods of VAWT

As explained in the latter subsection, it is crucial to be able to simulate the behaviour of a VAWT before it is manufactured. Doing this allows, among others, to have a view on the power produced by the wind turbine in different conditions, as well as on its wake. In the case of a wind farm, being able to model the wake of a wind turbine becomes essential.

A key point of attention in numerical simulations is to find the right trade-off between the accuracy and the cost. Doing complete simulations with a very high accuracy will require a lot of time in addition to important computational resources which leads to important costs.

A lot of strategies exist to simulate a VAWT. The easiest ones macroscopically consider the rotor as a device that captures energy from the wind, whereas the most complicated ones simulate the whole flow surrounding the wind turbine in addition to the VAWT that is modelled into details. These models that simulate the flow obviously have to take into account the turbulence to be exact and useful. Three main strategies, which are briefly detailed below, are nowadays widely used in order to simulate a flow with turbulence. The informations present in this subsection are mainly coming from [22].

- **Direct Numerical Simulation (DNS)**

  In this way of modelling, the Navier-Stokes equations are directly solved without using any model to manage the turbulence. Therefore, the mesh size has to be very small in order to capture the small scales of turbulence. This leads to very long and expensive simulations that are still not able to simulate high-velocity and complex flows today.

- **Large Eddy Simulation (LES)**

  In this method, a spatial filter is applied and only the large scale structures of turbulence are simulated while the others are only modelled. This supposes that the behaviour of the small scale structures is isotropic whereas the behaviour of the larger scale structures is influenced by the surroundings, anisotropic and depends on its history. The size of the mesh is in general set equal to the size of the filter and is by far larger than the Kolmogorov scale. This method thus loses more information than the DNS but is more time and cost efficient.

- **Reynolds-Averaged Navier-Stokes Simulation (RANS)**

  The Reynolds-Averaged Navier-Stokes Simulation is dealing with averaged flow, i.e. the idea of instantaneous disappears. Solving the small scale structures is thus not a problem anymore and the mesh size increases considerably. Hence, this approach seriously reduces the computational cost, but is at the same time less accurate.

The two codes that solve the flow around a VAWT developed at UCLouvain, BigFlow (see chapter 3) and VPM (see [7]) are using the LES method.

Then, the VAWT itself has to be modelled and several models exist to this end. For the sake of conciseness, only the VAWT simulation methods that are relevant for this work will briefly be presented below.

1.3.1 Double Multiple Stream Tube (DMST)

The double stream tube model is a momentum method which enjoys a limited computational cost. This model originates from the Single Stream Tube (SST) in which the swept area of the rotor is considered as a simple actuator surface. The idea is to equate the forces on the blades to the change in momentum through the turbine. The DMST additionally proposes to separate the swept area in different actuator surfaces (i.e. multiple stream tubes) and to put two actuator surfaces for each stream tube, one upwind and one downwind to account for the fact that the wind crosses the vertical axis wind turbine two times. It should be noted that in order to respect the mass flow conservation, the stream tubes can expand, as shown in figure 1.3. [3]

Even if its low computational cost may seem attractive, the DMST suffers from a lack of accuracy compared to more complete methods. For example, the influence of the downwind part of the flow on the upwind part is totally neglected. [37]

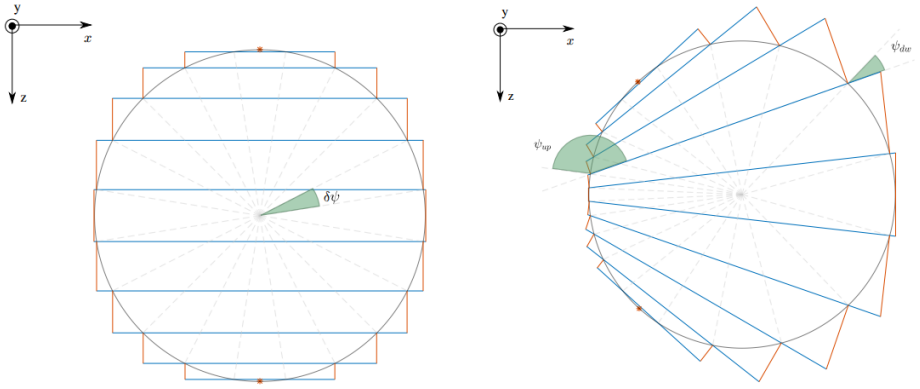

Figure 1.3: The concept of DMST, with and without expansion [9]

1.3.2 Immersed lifting lines in a Vortex-particle mesh method (VPM)

This method was developed at UCLouvain (see [7]) in 2017 and combines a vorticity-velocity formulation of the equations of Navier-Stokes with immersed lifting lines. This hybrid method solves the advection with particles while the classical right-hand side of the equations including the Poisson equation is evaluated on a grid. High order interpolation schemes are then used to match these two different approaches. The generation of vorticity along the blades is then added through immersed lifting lines that rely on the Kutta-Joukowski theorem. [7]

VPM has shown excellent results and will therefore serve as a reference in this work [7].

1.3.3 Actuator Cylinder Model (ACM)

The actuator cylinder model was developed by Madsen (see [20]) and extends the concept of the actuator disk to the area of the cylinder that represents the VAWT, as shown on figure 1.4. The ACM is used in the frame of a flow solver (as it is the case here with BigFlow, see chapter 3 for more details) and is made of three main steps : firstly, to determine the velocity at each grid point of the cylinder, secondly, to compute the forces applied by the blades on the flow with the help of aerodynamics and thirdly to apply these forces on the flow. [8],[37]

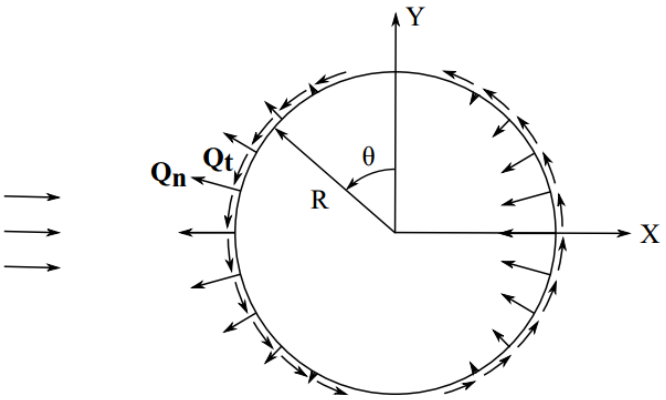

Figure 1.4: The concept of ACM [8]

1.3.4 Actuator Line Model (ALM)

The actuator line model, originally developed by Sorensen en Shen (see [32]), globally follows the same idea as the ACM except that the wind turbine is modelled by lines of control points, representing the blades. The three main steps stay more or less the same : interpolation of velocities from the flow on the actuator lines, computation of the forces using blade element theory and at last, distribution of the forces on the grid points of the flow near the actuator lines locations. [34],[1]

1.4 Dynamic stall

When a blade undergoes a too large angle of attack, the boundary layer detaches and the lift force stalls; this is the static stall phenomenon. However, when the same blade encounters large and relatively quick variations of angle of attack, it stalls again and again. This leads to an increase of the lift force due to a delay of stall and is known as the dynamic stall. Figure 1.5 compares the lift coefficient curves of a mid-blade VAWT point : the blue curve represents the case in which the dynamic stall is not taken into account while the red curve shows the influence of the dynamic stall. When the blade reaches the static stall angle of attack of 14°, it stalls in the static case and it further produces lift in the dynamic case. Physically, after the separation of the boundary layer on the extrados, a dynamic stall vortex will build up on the leading edge of the blade and will then detach and travel down to the trailing edge, resulting in the observed increment of lift. Once the dynamic stall vortex has left the blade, the stall occurs and the flow then reattaches itself when the angle of attack diminishes again. More details on the physics can be found in chapter 2. [30]

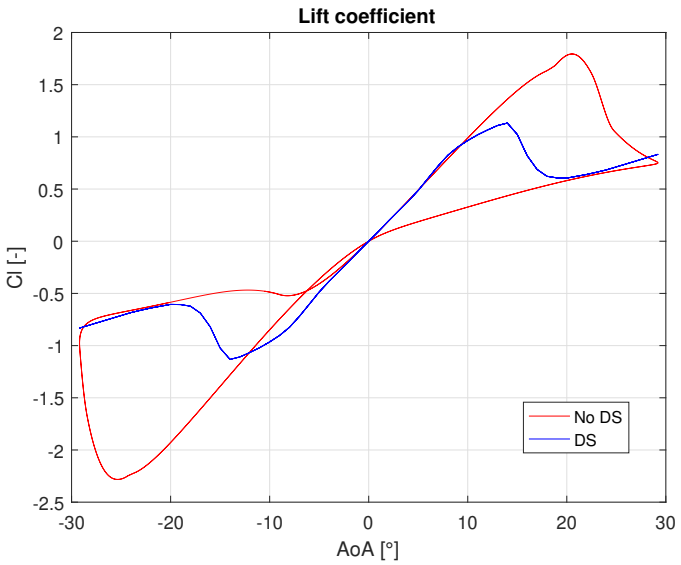

Figure 1.5: General look comparison between static and dynamic stall in the context of a VAWT

The dynamic stall has first been modelled by Beddoes (see [4]) in the case of helicopter aerodynamics in the early 80's [13]. Together with Leishman, they strove to develop semi-empirical models to represent this complex phenomenon. Later on, other models emerged and some of them were specifically adapted to vertical axis wind turbine. Indeed, when the TSR of a VAWT is not too high, the blades cyclically pass the static stall angle of attack and dynamic stall has the opportunity to develop [30]. Therefore, being able to simulate this dynamic stall in the context of vertical axis wind turbines appears to be crucial to obtain correct models, especially because experiences have shown that taking this phenomenon into account could lead to substantial increases in terms of VAWT power (see section 4.3.2).

1.5 Objectives and outlines

The main goal of this thesis is to investigate the complex phenomenon of dynamic stall in the cases of an actuator cylinder model as well as an actuator line model in the context of vertical axis wind turbines.

To this end, different models of dynamic stall were studied and the third generation of the Leishman-Beddoes model (LB model) was implemented on the existing codes of ALM and ACM. The flow solver coupled with these methods is a fourth-order finite difference code, which was developed by Duponcheel [12].

The model of dynamic stall is first validated on a pitching blade, before being tested using the constants of previous works done at UCLouvain in order to be fairly compared for different TSRs with a VPM method and a DMST method. After that, the LB model is even refined in order to better respect the behaviour of the tangential forces and to compare ALM and ACM in a uniform flow. To end with, ALM and ACM are compared in a turbulent flow.

More specifically :

Chapter 2 In this chapter, the dynamic stall is developed theoretically. After some explanations on the phenomenology, some of the most important models that currently exist to model the dynamic stall are briefly presented and the choice of the LB model is justified. After that, the LB model is explained mathematically : first, the original version of the model is detailed. The modifications in the third generation of the model are then specified, before the modifications to these two models are explained and justified. At last a subsection will describe how to obtain the multiple constants of these models.

Chapter 3 The third chapter focuses on the implementation of the chosen theoretical model of dynamic stall in the codes of ALM and ACM. The latter are detailed as well as the choices and the specificities required by both models for the implementation. The flow solver is also briefly described.

Chapter 4 The results are exposed here. First, the validation of the model on a simple pitching blade is presented. Secondly, the set-up of all the simulations is defined, thanks to a convergence analysis. Thirdly, a transverse comparison between ALM, ACM, DMST and VPM is carried out for different TSRs in terms of forces and wakes. Fourthly, the results of the simulations for ALM and ACM in a uniform flow are analyzed for one specific TSR. At last, the same comparison is carried out with a turbulent inflow.

Chapter 5 The last chapter concludes this work with a summary of the main results and perspectives for further research.

Chapter 2

Modelling the dynamic stall

The dynamic stall, briefly introduced in section 1.4, arises when an airfoil undergoes quick changes in its angle of attack and when this angle of attack overwhelms the static stall value of the angle of attack. It has a crucial influence on the force curves and as a consequence on the power produced in vertical axis wind turbines. Indeed, as the blades of a VAWT are facing the wind in all the directions, their angle of attack will undergo large changes from negative to positive values in a repetitive way depending on the rotational speed. The dynamic stall also arises in the case of helicopter aerodynamics and the first models were developed with that application in mind [17]. Several models have been developed in order to better handle it in the numerical simulations of VAWTs. This chapter aims at shedding some light on the behaviour of the dynamic stall and the way to model it. First the phenomenology of the dynamic stall is presented. Then the different models used to represent this phenomenon are introduced. At last, the Leishman-Beddoes model of dynamic stall is explained.

2.1 Phenomenology

Although several studies, both numerical and experimental, have already been carried out on the phenomenon of dynamic stall, the latter is not yet fully understood [30]. However, previous works have been done in order to represent and explain it at best. On figure 2.1, the lift and drag coefficients of the static (dotted) and dynamic stall (solid) are compared. For the static stall, the lift increases until the angle of attack reaches a critical value where the boundary layer will detach and make the lift dropping. It could be observed that in the case of the dynamic stall, the onset of stall lift is delayed and the lift coefficient is able to reach a higher maximal value than in the static case. As the range of angles of attack seen by the blades is larger at low TSR, the influence of the dynamic stall will be more important for small TSR [13]. Following Leishman [19], the dynamic stall phenomenon can be decomposed into five different parts (see figure 2.1). These five steps are derived from [19] and adapted with the further explanations of [23], [30], [2] and [17].

1. First, as the value of the angle of attack increases quickly, a vortex is shed into the wake (*starting vortex*) when the value of the angle of attack exceeds the value of the static stall angle of attack. This results into a less adverse pressure

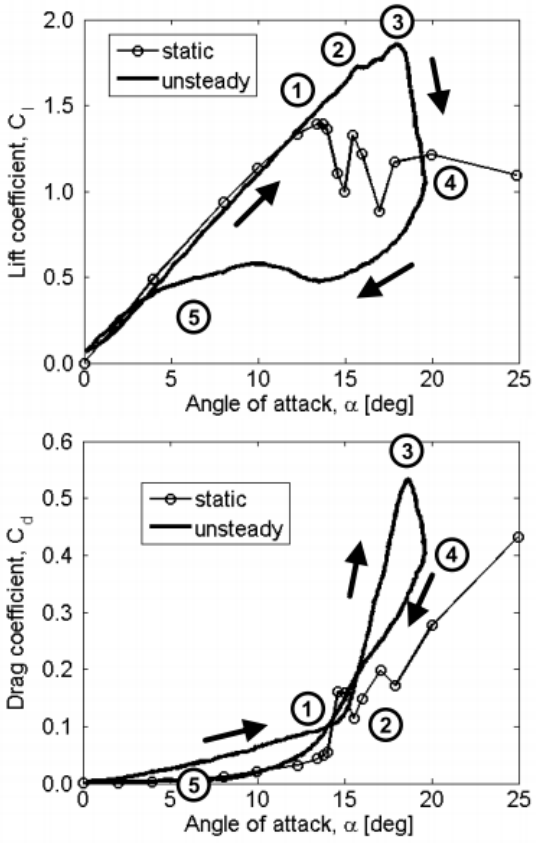

Figure 2.1: Behaviour of an oscillating airfoil [19]

gradient along the chord compared to the pressure gradient at an identical angle of attack under quasi-steady conditions and an unsteady reduced angle of attack. As a consequence, the flow reverses into the boundary layer and the onset of the separation of the flow is delayed.

2. As the angle of attack continues to increase, the separation point comes closer to the leading edge of the airfoil and the boundary layer eventually detaches from it. This boundary layer rolls up to form a vortex at the leading edge, called the *dynamic stall vortex*. This vortex located on the suction side provides an additional lift coefficient.

3. Between stage 2 and 3, the vortex builds up in strength and convects from the leading edge to the trailing edge at a velocity that is experimentally estimated to be between one third and one half of the upstream velocity U_∞. The convection of this dynamic stall vortex along the suction side provides a light lift increment as well as a tremendous drag increase.

4. At the end of stage 3 or at the beginning of stage 4 depending on the references, the dynamic stall vortex is ejected from the suction side at the trailing edge. Instantaneously, the airfoil stalls and the lift hence plunges to reach lower values than the static ones at the same angle of attack. The flow is then completely detached.

5. At last, when the angle of attack becomes low enough, the boundary layer reattaches on the suction side. Before that, the lift coefficient stays well beyond the coefficients of static lift whereas the drag coefficient follows the static curve.

2.2 Different models

Different models exist in order to represent the dynamic stall phenomenon at best. According to Larsen *et al.* (2007) these models can be categorized into three main classes:

1. The first class of models tries to mathematically represent all the different physical phenomenons developed in the former section : the events that the flow undergoes are described. For example, a lift reduction is implemented when the vortex is ejected. These models aim to represent the effects of the flow conditions.

2. The second group of models only focuses on the aerodynamic curves. Their characteristics are modelled without taking the physics into account that much. For example, at a certain angle of attack, an established drop in lift coefficient will be implemented.

3. The third way of thinking to model the dynamic stall is to only modify the angle of attack in order to get a dynamic angle of attack.

In what follows, a non-exhaustive list of the most famous and commonly used models is briefly presented.

- The Leishman-Beddoes model belongs to the first category of models. It aims at representing the physics of dynamic stall phenomenon e.g. by inserting some delays corresponding to physical events like the convection of the dynamic stall vortex. It has been derived with the purpose of better treating the aerodynamic of helicopters [17]. This model splits the dynamic stall into three categories : the unsteady attached flow, the unsteady separated flow and the dynamic stall vortex [23]. As the Leishman-Beddoes model was chosen to be implemented in this work, it will be further addressed in the following section (2.3).

- The ONERA method was developed by Tran and Petot (1981) and falls in the second category of models. In this model, the load coefficients are described by means of a third-order differential equation [17]. The differential equation is splitted into two domains depending on the angle of attack : at low values the model will be linear, which will no longer be the case when the angle of attack increases [17].This method uses 18 empirical coefficients exclusively determined experimentally. Although this method performs quite good, it still encounters difficulties to perfectly shape the flow reattachment [2].

- The Boeing-Vertol model, developed by Tarzanin (1972), is based on a relation between a dynamic stall angle of attack and the static stall angle : a dynamic stall angle of attack is determined by this relation and the interpolation of the static data provides the load coefficients [17]. It therefore obviously belongs to the third category of models.

- The model defined by Øye (1991) uses a simple first order filter in order to find out the position of the separation point f and then computes the dynamic stall effects from this position [2]. It omits the transient effects of the attached flow [17]. Despite this lack of accuracy, this method has been popular thanks to its good results and its relative simplicity [2].

- The Sheng model follows the same way of thinking than the Leishman-Beddoes model but is more sophisticated. Compared to the LB model, two major modifications can be highlighted : the condition for dynamic stall onset is changed and the coefficient of normal force is calculated differently [23]. The Sheng model is computationally heavier than the other methods presented here but it has the advantage to be very accurate [2].

2.3 Leishman-Beddoes model

The Leishman-Beddoes model is a semi-empirical model mainly developed by Leishman and Beddoes between the end of the 70's and the beginning of the 90's that represents the physics of the dynamic stall. This model aims to reproduce the aerodynamic curves from polars in uniform and steady flows. The original model of Leishman-Beddoes was developed for compressible flows (Mach number being greater than 0.3) but adaptations exist for incompressible flows. [6]

Among all the existing models, the LB model was chosen in this work for several reasons. First of all, as already mentioned earlier, the Leishman-Beddoes model is a semi-empirical model, which means that it takes the physics of the dynamic stall phenomenon into account. As a semi-empirical model, its purpose is not to perfectly capture all the flow characteristics but rather to focus on the main points and to wrap them up in an efficient and fast way [17]. In addition, opposite to the ONERA model for example, the Leishman-Beddoes model involves quite a few empirical constants and still provides good results [2]. Furthermore, the Leishman-Beddoes model is very popular and has been widely used, resulting in a lot of previous validations of the results [2]. At last, the LB model was used in the VPM simulations of VAWTs processed at UCLouvain [7] and in order to make fair comparisons with these results, the LB model was an interesting choice.

The original version of the Leishman-Beddoes model is first presented here. The more precise third generation of the model developed by Beddoes in 1993 is then detailed, before the modifications of the third-generation model implemented in the code used for the simulations are explained. As the third-generation model is highly based on the original one, it is worth to first present the original model and then to highlight the modifications. The following developments are mainly taken from the work of Dyachuk *et al.* (2014) which is overlapped by other sources ([23],[6], [30],[2],[5]). Additional information from other sources will be mentioned in the text itself.

2.3.1 Prerequisite

Before going through these three parts and as the LB model acts on the normal and tangential forces coefficients C_n and C_t, some parameters have to be defined.

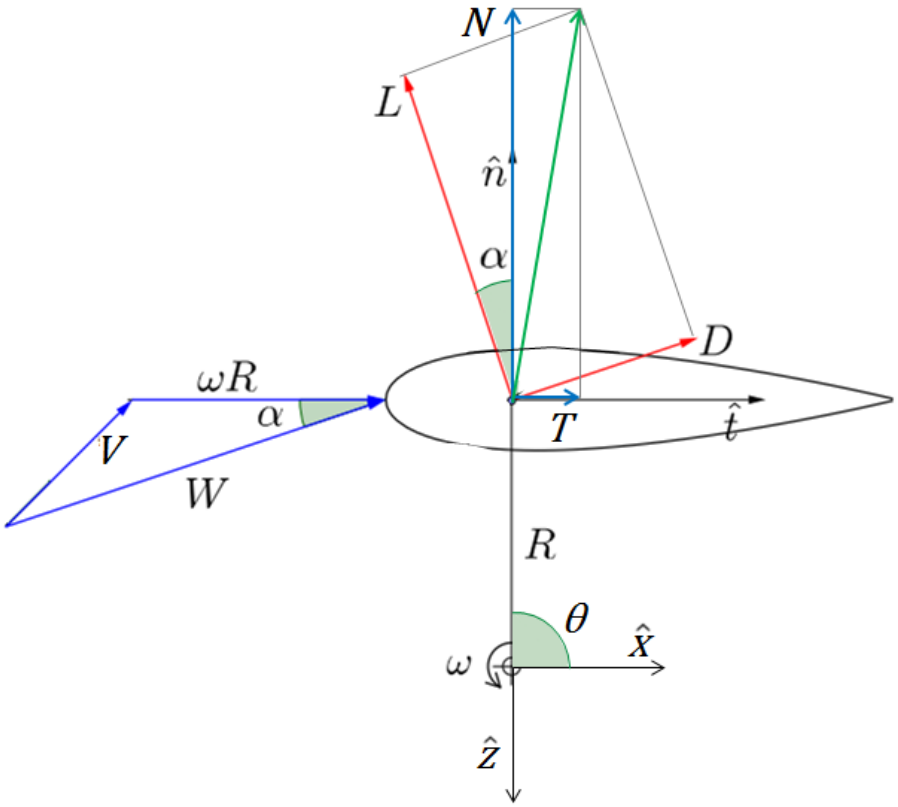

Figure 2.2: Parameters of the flow around a VAWT blade, adapted from [11]

Figure 2.2 depicts the different angles, velocities and forces of interest for a rotating blade section of a vertical axis wind turbine. Two systems of coordinates are applying on this scheme, one (x, y, z) for the VAWT and the other (n, y, t) for the blade considered here. $\overrightarrow{V}$ is the incident flow velocity with components v_x and v_z that can be translated in the blade coordinate system following :

$$v_n = v_x \cos\theta - v_z \sin\theta \tag{2.1}$$
$$v_t = v_x \sin\theta + v_z \cos\theta \tag{2.2}$$

$\overrightarrow{W}$ represents the relative velocity of the wind with respect to the blade which has to take into account the rotation of the VAWT at an angular velocity ω :

$$\overrightarrow{W} = v_n \overrightarrow{n} + (v_t + \omega R) \overrightarrow{t} \tag{2.3}$$

The angle of attack α is therefore defined as :

$$\alpha = \arctan\left(\frac{v_n}{v_t + \omega R}\right) \tag{2.4}$$

L and D respectively stand for the lift and drag forces while N and T stand for the normal and tangential forces. C_l, C_d, C_n and C_t are the coefficients associated with these forces after adimensionalisation has been carried out. The Leishman-Beddoes model finds the coefficients C_n and C_t and the lift and drag coefficients can hence easily be found using :

$$C_l = C_n \cos\alpha + C_t \sin\alpha \tag{2.5}$$
$$C_d = C_n \sin\alpha + C_t \cos\alpha + C_{d,0} \tag{2.6}$$

where $C_{d,0}$ is the drag coefficient at zero angle of attack.

2.3.2 Original version

The LB model can be divided into three sections : the first one models the unsteady attached flow, the second one strives to represent the unsteady separated flow and the last one models the dynamic stall vortex.

2.3.2.1 Unsteady attached flow

The solution for unsteady attached flow is divided into two components : an impulsive component and a circulatory component. The circulatory component is due to the bound vortex on the suction side and grows with the increase of angle of attack, it is given by :

$$C^C_{n_k} = C_{n_a} \cdot \alpha_{e_k} \tag{2.7}$$

where C_{n_a} is the slope of the normal force coefficient in static conditions at $\alpha = 0$ and α_{e_k} is an equivalent angle of attack which will be computed in the following equations. The index k reflects the time evolution of the coefficients. The equivalent angle of attack comprises the geometric angle of attack diminished by two deficiency functions X_k and Y_k. This equivalent angle of attack contains all the informations of the upstream flow and takes the effects of the shed wake into account[6].

$$\alpha_{e_k} = \alpha_k - X_k - Y_k \tag{2.8}$$

$$\begin{cases} X_k = X_{k-1}\ \exp(-b_1\beta\Delta s) + A_1\ \Delta\alpha_k\ \exp\left(\dfrac{b_1\beta\Delta s}{2}\right) \\ Y_k = Y_{k-1}\ \exp(-b_2\beta\Delta s) + A_2\ \Delta\alpha_k\ \exp\left(\dfrac{b_2\beta\Delta s}{2}\right) \end{cases} \tag{2.9}$$

where b_1, b_2, A_1 and A_2 are constants given in 2.3.5, $\Delta\alpha_k$ is the change in angle of attack regarding the previous time step : $\Delta\alpha_k = \alpha_k - \alpha_{k-1}$, and $\beta = 1 - M^2$, M being the Mach number. Δs is the non-dimensional time step, that will be used in the whole model and which is defined in equation 2.10. It represents the covered distance on the profile at a velocity $\|\overrightarrow{W}\|$ (i.e. the norm of the vector representing the relative velocity of the wind with respect to the blade) corresponding to the time step Δt and is adimensionalized by the half-chord $\frac{c}{2}$.

$$\Delta s = \frac{2\|\overrightarrow{W}\|\Delta t}{c} \tag{2.10}$$

The impulsive component is due to a quick change in angle of attack that will cause local changes of pressure, but tends to disappear quite rapidly [2]. It is defined by :

$$C_{n_k}^I = \frac{4K_a T_I}{M}\left(\frac{\Delta\alpha_k}{\Delta t} - D_k\right) \tag{2.11}$$

where $K_a = \frac{0.75}{1-M+\pi(1-M^2)M^2(A_1b_1+A_2b_2)}$ and $T_I = \frac{c}{a}$, a being the speed of sound. D_k is a deficiency function which evolves as follows:

$$D_k = D_{k-1}\ \exp\left(-\frac{\Delta t}{K_a\, T_I}\right) - \left(\frac{\Delta\alpha_k - \Delta\alpha_{k-1}}{\Delta t}\right)\ \exp\left(-\frac{\Delta t}{2\, K_a\, T_I}\right) \tag{2.12}$$

Wrapping it all, the normal force coefficient under unsteady attached flow is given by the sum of the circulatory and the impulsive components :

$$C_{n_k} = C_{n_k}^C + C_{n_k}^I \tag{2.13}$$

It should be noted that the major contribution to this normal force coefficient is the circulatory component, to the extent that the impulsive component could be neglected [6].

2.3.2.2 Unsteady separated flow

The second part of the Leishman-Beddoes model is sometimes divided into two subsections : one for the leading edge separation and one for the trailing edge separation. It should be noted that the trailing-edge separation chronologically occurs before the leading-edge separation, but the condition for the latter will first be derived.

Leading-edge separation

First of all, it has been remarked that a delay in the pressure response appears in unsteady conditions. This can be fixed by adding a first-order lag to the normal force coefficient C_n :

$$C'_{n_k} = C_{n_k} - D^p_k \tag{2.14}$$

where D^p_k is another deficiency function given by :

$$D^p_k = D^p_{k-1} \exp\left(\frac{-\Delta s}{T_p}\right) + (C_{n_k} - C_{n_{k-1}}) \exp\left(\frac{-\Delta s}{2\,T_p}\right) \tag{2.15}$$

T_p is the adimensional time constant associated with this delay whose value can be found in the dedicated section below.

The value of the angle of attack is also delayed due to the unsteady conditions and a new value which takes the lag into account is derived :

$$\alpha'_k = \frac{C'_{n_k}}{C_{n_a}} \tag{2.16}$$

The leading-edge separation condition can then be derived : indeed, when C'_{n_k} exceeds the critical normal force coefficient C_{n_1}, the dynamic stall vortex is formed. The value of C_{n_1} is based on the static polar data and is further explained in section 2.3.5. In order to take the negative values of angle of attack into account, the absolute value has to be taken, which leads to :

$$|C'_{n_k}| > C_{n_1} \Rightarrow \textit{Dynamic Stall} \tag{2.17}$$

It should be noted that this condition also holds for the reattachment of the boundary layer i.e. if $|C'_{n_k}| < C_{n_1}$.

Trailing-edge separation

From Kirchoff-Helmoltz's theory, it is known that the aerodynamic coefficients can be acquired on a profile using the position of the separation point of the boundary layer [30]. This position is monitored by a function f', as shown on figure 2.3. Once this function f' is found, it will then be possible to obtain C_n and C_t.

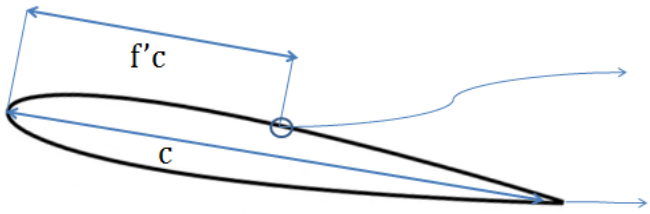

Figure 2.3: Position of the separation point

Leishman and Beddoes decide to approximate f' with the two following exponential relations :

$$f'_k = \begin{cases} 1 - 0.3 \, \exp\left(\frac{|\alpha'_k| - \alpha_1}{S_1}\right) & |\alpha'_k| < \alpha_1, \\ 0.04 + 0.66 \, \exp\left(\frac{\alpha_1 - |\alpha'_k|}{S_2}\right) & |\alpha'_k| \geq \alpha_1 \end{cases} \tag{2.18}$$

where S_1 and S_2 are constants to be defined (see section 2.3.5) and α_1 corresponds to the static stall angle of attack.

Due to the unsteady conditions, the boundary layer itself needs to be lagged and this is done with the new deficiency function D_k^f.

$$f''_k = f'_k - D_k^f \tag{2.19}$$

$$D_k^f = D_{k-1}^f \, \exp\left(\frac{-\Delta s}{T_f}\right) \, + \, (f'_k - f'_{k-1}) \, \exp\left(\frac{-\Delta s}{2 \, T_f}\right) \tag{2.20}$$

where T_f is a new constant.

Hence, the normal force coefficient for the dynamic separation point can be derived thanks to the Kirchoff's flow approximation to which the impulsive component of the normal force coefficient is added :

$$C_{n_k}^f = C_{n_a} \, \alpha_{e_k} \left(\frac{1 + \sqrt{f''_k}}{2}\right)^2 + C_{n_k}^I \tag{2.21}$$

2.3.2.3 Dynamic stall vortex

As stated in the previous subsection, the leading-edge separation occurs when the stall condition derived in equation 2.17 is met. The boundary layer rolls up to form the dynamic stall vortex which is continuously fed. This vortex then convects down to the trailing edge at a speed depending on the relative speed of the wind with respect to the blade [19]. Leishman and Beddoes have noticed that no major changes arise in the force distribution when the vortex is building up. However, when it detaches and starts to shed, this vortex provides an additional lift C_{v_k} which has to be implemented. This overshoot depends on the circulatory component of the normal force coefficient $C_{n_k}^C$ and on the delayed separation point :

$$C_{v_k} = C_{n_k}^C \left(1 - \left(\frac{1 + \sqrt{f''_k}}{2}\right)^2\right) \tag{2.22}$$

The total normal force coefficient then has two possibilities : either it decays exponentially with time and is updated by the new vortex lift C_{v_k} when the dynamic stall vortex is still on the profile, or it rapidly diffuses when the vortex has passed the trailing edge. It is hence quite important to track the position of the vortex on the airfoil. The adimensional time τ is used to this end : $\tau = 0$ at the leading edge separation, it then evolves with the adimensional time s and reaches the value $\tau = T_{VL}$ when the vortex is at the trailing edge.

Wrapping up all these informations gives :

$$C^v_{n_k} = \begin{cases} C^v_{n_{k-1}} \exp\left(\frac{-\Delta s}{T_v}\right) + (C_{v_k} - C_{v_{k-1}}) \exp\left(\frac{-\Delta s}{2\,T_v}\right) & 0 < \tau \leq T_{VL} \\ C^v_{n_{k-1}} \exp\left(\frac{-\Delta s}{T_v}\right) & \tau > T_{VL} \end{cases} \tag{2.23}$$

where T_v is another constant which is discussed in section 2.3.5.

It is also possible that multiple vortices develop i.e. after an adimensional time T_{st} since the dynamic stall vortex has passed the trailing edge, the time τ is reset and therefore allows to build another vortex with the equation 2.23. The time T_{st} corresponds to the effective Strouhal number and is given by :

$$T_{st_k} = \frac{2\,(1 - f''_k)}{0.19} \tag{2.24}$$

The last important point concerning the vortex shedding representation in the original Leishman-Beddoes model is that the absolute value of angle of attack must increase to obtain the overshoot in lift due to the vortex [5]. In other words :

$$|\alpha_n|\, decreases \;\Rightarrow\; C^v_{n_k} = 0 \tag{2.25}$$

At last, the normal force coefficient is obtained by superposing the coefficient $C^f_{n_k}$ due to the evolution of the separation point and the coefficient $C^v_{n_k}$ due to the dynamic stall vortex :

$$C_{n_k} = C^f_{n_k} + C^v_{n_k} \tag{2.26}$$

The tangential force coefficient is given by the following relations :

$$C_{t_k} = \begin{cases} \eta\, C_{n_\alpha}\, \alpha^2_{e_k}\, (f''_k)^{1.5} & f''_k < 0.7 \\ \eta\, C_{n_\alpha}\, \alpha^2_{e_k}\, \sqrt{f''_k} & otherwise \end{cases} \tag{2.27}$$

where η is the efficiency factor to emphasize the fact that even if the flow does not separate, the tangential force coefficient does not reach the value reached in a potential flow. Its value can be found in the section 2.3.5.

2.3.3 3G version

The third generation of the LB model is obviously more accurate than the original version. Only the differences with the original model detailed in the previous section are then highlighted here. Like before, these developments still mainly follow the work of Dyachuk *et al* (2014) and other references are explicitly mentioned.

2.3.3.1 Unsteady attached flow

The normal force coefficient is still composed of a circulatory and an impulsive component, but these are defined differently than in the original model. There are now three deficiency functions for α_e :

$$\alpha_{e_k} = \alpha_k - X_k - Y_k \tag{2.28}$$

$$\begin{cases} X_k = X_{k-1} \exp\left(\dfrac{-\beta\Delta s}{T_1}\right) + A_1 \left(\eta_{L_k} - \eta_{L_{k-1}}\right) \exp\left(\dfrac{-\beta\Delta s}{2T_1}\right) \\ Y_k = Y_{k-1} \exp\left(\dfrac{-\beta\Delta s}{T_2}\right) + A_2 \left(\eta_{L_k} - \eta_{L_{k-1}}\right) \exp\left(\dfrac{-\beta\Delta s}{2T_2}\right) \\ Z_k = Z_{k-1} \exp\left(\dfrac{-\beta\Delta s}{T_3}\right) + A_3 \left(\eta_{L_k} - \eta_{L_{k-1}}\right) \exp\left(\dfrac{-\beta\Delta s}{2T_3}\right) \end{cases} \tag{2.29}$$

where A_1, A_2, A_3, T_1, T_2 and T_3 are constants defined in section 2.3.5 and η_{L_k} is defined as the forcing term for the pitching motion around the profile quarter-axis.

$$\eta_{L_k} = \alpha_k + \frac{c}{2\|\overrightarrow{W}\|}\,\dot{\alpha_k} \tag{2.30}$$

The impulsive component of the normal force coefficient is also modified as follows:

$$C^I_{n_k} = \frac{4}{M}\,H_k \tag{2.31}$$

with

$$H_k = H_{k-1} \exp\left(\frac{-\Delta t}{T_I}\right) + \left(\lambda_{L_k} - \lambda_{L_{k-1}}\right) \exp\left(\frac{-\Delta t}{2T_I}\right) \tag{2.32}$$

where T_I is modified to become equal to $\frac{c(1+3M)}{4a}$. λ_{L_k} is the equivalent of η_{L_k} and is represented in the same way, except for one factor :

$$\lambda_{L_k} = \frac{\pi}{4}\left(\alpha_k + \frac{c}{4\|\overrightarrow{W}\|}\,\dot{\alpha_k}\right) \tag{2.33}$$

The rest of the reasoning for the unsteady attached flow is the same as in the original model.

2.3.3.2 Unsteady separated flow

Everything regarding the separation at the leading-edge does not change (the stall condition remains the same among others). Regarding the trailing-edge separation, the way to define the separation point slightly changes :

$$f'_k = \begin{cases} 1 - 0.4\ \exp\left(\frac{|\alpha'_k| - \alpha_1}{S_1}\right) & |\alpha'_k| < \alpha_1, \\ 0.02 + 0.58\ \exp\left(\frac{\alpha_1 - |\alpha'_k|}{S_2}\right) & |\alpha'_k| \geq \alpha_1 \end{cases} \tag{2.34}$$

The breakpoint which corresponds to the point where f'' is evaluated at the static stall angle α_1 is moved from 0.7 to 0.6.

The position of the separation point f' is still delayed and the deficiency function D_k^f is still computed using 2.20, but in the 3G-model, the way to handle the dynamic stall vortex is seen quite differently.

2.3.3.3 Dynamic stall vortex

Indeed, a modulation parameter V_x is introduced here and it will have a crucial effect on the new position of the separation point :

$$f_{3G_k} = f''_k - D_k^f\, V_{x_k} \tag{2.35}$$

where V_x is defined as :

$$V_x = \begin{cases} \left(\sin\left(\frac{\pi\tau}{2T_{VL}}\right)\right)^{\frac{3}{2}} & 0 < \tau \leq T_{VL} \\ \left(\cos\left(\frac{\pi(\tau - T_{VL})}{T_v}\right)\right)^2 & \tau > T_{VL} \end{cases} \tag{2.36}$$

The advantage of using this method is that the multiple-vortex shedding phenomenon is already taken into account in V_x thanks to its periodicity.

As in the original model, the absolute value of angle of attack should absolutely increase to obtain the overshoot in lift due to the vortex [5]. This is translated here with :

$$|\alpha_n|\ decreases\ \Rightarrow\ V_x = 0 \tag{2.37}$$

At last, the values for the normal and tangential forces coefficients can be obtained:

$$C_{n_k} = C_{n_a}\ \alpha_{e_k}\ \left(\frac{1 + \sqrt{f_{3G_k}}}{2}\right)^2 + C_{n_k}^I \tag{2.38}$$

$$C_{t_k} = \begin{cases} \eta\, C_{n_\alpha}\ \alpha_{e_k}^2\ (f''_k)^{1.5} & f''_k < 0.6 \\ \eta\, C_{n_\alpha}\ \alpha_{e_k}^2\ \sqrt{f''_k} & otherwise \end{cases} \tag{2.39}$$

2.3.4 Modifications

Whereas the dynamic stall model implemented in this work is highly based on the third-generation Leishman-Beddoes model, some modifications have been carried out in order to obtain better results.

Firstly, in order to better handle the flows with low Mach numbers, which is the case for the VAWTs, a supplementary lag is added at C'_{n_k} [23] :

$$C''_{n_k} = C'_{n_k} - D^b_k \tag{2.40}$$

$$D^b_k = D^b_{k-1} \exp\left(\frac{-\Delta s}{T_b}\right) + (C'_{n_k} - C'_{n_{k-1}}) \exp\left(\frac{-\Delta s}{2\,T_b}\right) \tag{2.41}$$

This correction induced a new constant T_b whose value can be found in the following section.

Secondly, another modification was carried out on equation 2.36 by [23] to better model the increment of lift due to the dynamic stall vortex :

$$V_x = \begin{cases} \left(\sin\left(\frac{\pi\tau}{2T_v}\right)\right)^{\frac{3}{2}} & 0 < \tau \leq T_v \\ \left(\cos\left(\frac{\pi(\tau - T_v)}{T_{VL}}\right)\right)^2 & \tau - T_v < \frac{T_{VL}}{2} \\ 0 & \tau - T_v \geq \frac{T_{VL}}{2} \end{cases} \tag{2.42}$$

where T_v is the time during which the dynamic stall vortex forms itself and $\frac{T_{VL}}{2}$ is the time during which it convects downstream. $\tau = 0$ when the vortex appears, $\tau = T_v$ when it begins to convect and $\tau = T_v + \frac{T_{VL}}{2}$ when it reaches the trailing-edge.

Thirdly, following Pierce [6], it is better to use two different functions to model the position of the separation point. Indeed, as the relations 2.18 and 2.34 are fitted on the static polar of C_n, the previous relations to obtain the tangential force coefficient C_t don't perform well. As a solution, Pierce proposed to use two non-physical positions for the separation point f_n and f_t, which will be called the effective separation point positions. The constants related to these two functions are obtained by fitting the static polars of C_n and C_t, which is further explained in section 2.3.5.

$$f'_{n_k} = \begin{cases} 1 - 0.4 \exp\left(\frac{|\alpha'_k| - \alpha_1}{S_{1_n}}\right) & |\alpha'_k| < \alpha_1, \\ 0.02 + 0.58 \exp\left(\frac{\alpha_1 - |\alpha'_k|}{S_{2_n}}\right) & |\alpha'_k| \geq \alpha_1 \end{cases} \tag{2.43}$$

$$f'_{t_k} = \begin{cases} 1 - 0.4 \exp\left(\frac{|\alpha'_k| - \alpha_1}{S_{1_t}}\right) & |\alpha'_k| < \alpha_1, \\ 0.02 + 0.58 \exp\left(\frac{\alpha_1 - |\alpha'_k|}{S_{2_t}}\right) & |\alpha'_k| \geq \alpha_1 \end{cases} \tag{2.44}$$

Fourthly, it has been remarked that the equations to obtain C_t (2.39) do not allow to get a negative tangential force coefficient after the static stall angle of attack, while the physics show that this normally appears [30]. Many improvements have then been

proposed to fix this problem [6] and the solution of Urbina *et al* [35] was retained here after empirical testings were processed using the different methods. Also, the C_n coefficient was slightly changed according to [6].

$$C_n = C_{n\alpha} \cdot \sin\alpha \cdot \left(\frac{1+\sqrt{f_n}}{2}\right)^2 \tag{2.45}$$

$$C_t = \eta \cdot C_{n\alpha} \cdot \sin\alpha \cdot \tan\alpha \cdot \left(\sqrt{f_t} - E_0(1-\sqrt{f_t})^2\right) \tag{2.46}$$

The constant E_0 is obtained from the static polar fit, see section 2.3.5.

Using the right constants and without the dynamic effects, the coefficients C_n and C_t based on the separation point theory should normally fit the static airfoil data correctly. Figure 2.4 shows the differences between the 3G Leishman-Beddoes model, the fit obtained with the two last modifications done here and the static data. Thanks to the improvements, the behaviour of the tangential force coefficient is better respected and can reach negative values.

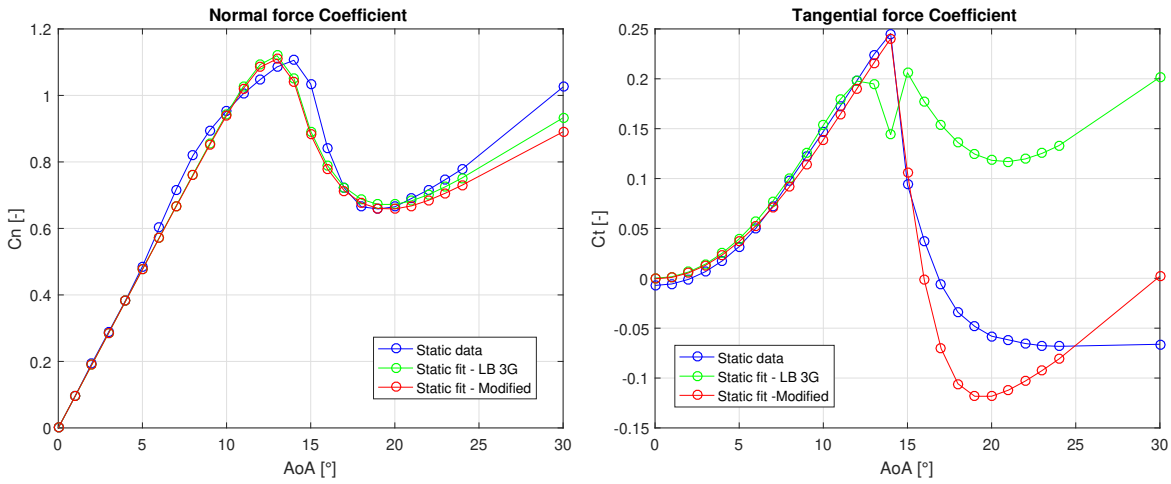

Figure 2.4: Improvement of the 3G LB model based on the static data fits

2.3.5 Constants

As seen before, a lot of constants are involved in the LB model. Some of them are coming from the static airfoil data whereas some of them are empirical.

2.3.5.1 Static constants

The constants coming from the static airfoil data depend then on the Reynolds number. A solution to manage this could be to obtain the different constants for various Reynolds numbers and then to interpolate between the known values when a blade encounters a flow at a Reynolds for which the constants have not been computed [13]. However, nothing says that the interpolation will provide good results, among others for the derivation of the S constants. The constants will only be derived here for the case of NACA0015 airfoil at a Reynolds of 680000. The data come from Sandia Labs, see [29].

- $\mathbf{C_{n\alpha}}$: $C_{n\alpha}$ corresponds to the slope of the normal force coefficient when the flow is attached. For the current case, it is equal to 5.4677 $[\frac{1}{rad}]$, as shown by the red curve on figure 2.5.

- $\mathbf{C_{n_1}}$: C_{n_1} is defined as the critical normal force coefficient, in other words the normal force coefficient corresponding to the static stall angle of attack. It is shown in green on figure 2.5 and equal to 1.106.

- $\boldsymbol{\alpha_1}$: α_1 is the static stall angle of attack, found with the black line on figure 2.5, equal to 14° here.

- $\mathbf{C_{d_0}}$: As the drag coefficient C_d is worth $C_n \sin\alpha - C_t \cos\alpha + C_{d_0}$, the zero angle of attack drag coefficient C_{d_0} should also be derived from the static polar data and is equal to 0.007138 (see figure 2.5).

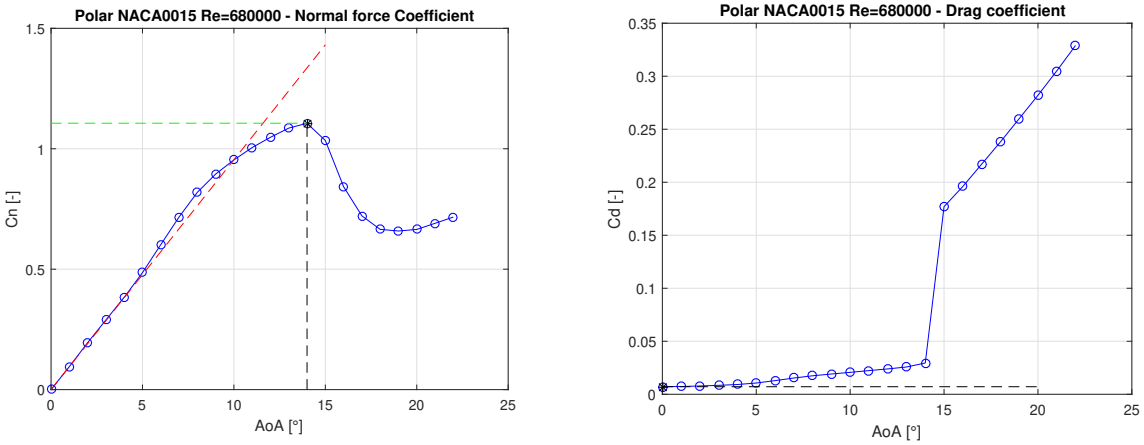

Figure 2.5: Static constants coming from the normal and drag force coefficients

- $\mathbf{S_1, S_2, S_{1_n}, S_{2_n}, S_{1_t}, S_{2_t}}$: The method proposed to find the constants S_1 and S_2 of the 3G LB model is to reorganize equations 2.34 to obtain graphs of S_1 and S_2 in function of the angle of attack using the relation 2.38 and the static polar data. However, as explained in the former section, this provides quite poor results when the constants are then plugged in the tangential force coefficient and when the latter is compared to the static airfoil data. Therefore, the constants S_1 and S_2 are found for the normal force case (S_{1_n}, S_{2_n}) and for the tangential case (S_{1_t}, S_{2_t}). The methodology is the same except that the tangential force coefficient is used for S_{1_t} and S_{2_t} here. The behaviour of all the S obtained are plotted on figure 2.6 and the goal is then to output constants from this. S_1 should be taken before the static stall angle of attack and S_2 should be taken after it. The choice is here done to take the mean of an arbitrary number of values which seem to stay constant (black-dotted on the graphs), resulting in the following values : $S_{1_n} = 0.02346[rad]$, $S_{2_n} = 0.02861[rad]$, $S_{1_t} = 0.15556[rad]$ and $S_{2_t} = 0.01777[rad]$.

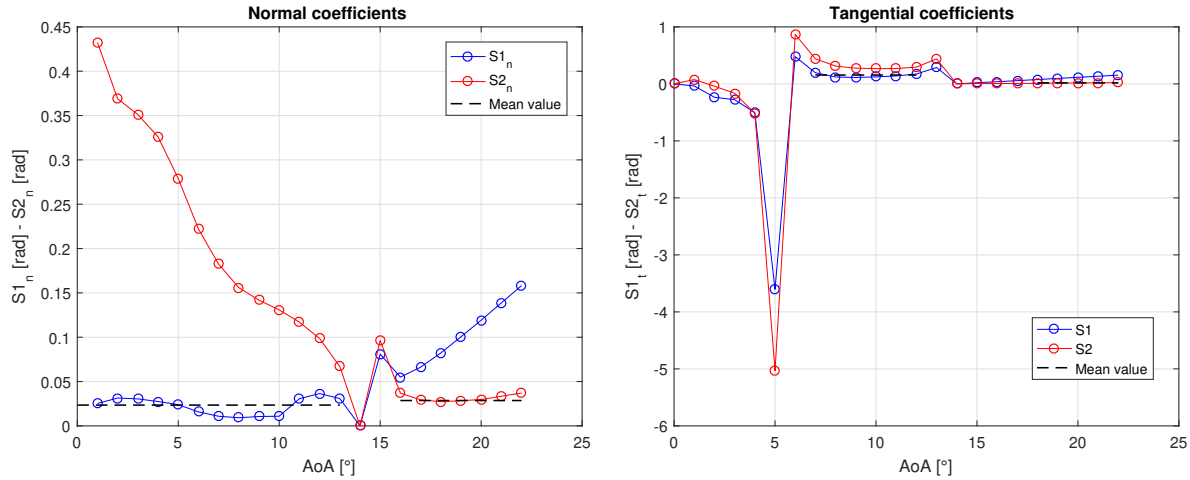

Figure 2.6: Obtention of S_{1_n}, S_{2_n}, S_{1_t} and S_{2_t}

- $\mathbf{E_0}$: E_0 is found empirically by trying to fit the static airfoil data at best with the equation 2.46 and is taken equal to 0.3.

2.3.5.2 Empirical constants

- $\mathbf{A_{1,2,3}}, \mathbf{b_{1,2}}, \mathbf{T_{1,2,3}}$: The following constants are independent of the Mach number and the chosen profile. They are found empirically and all the references used for this section ([2], [23], [6], [30], [5], [13]) agree with their values.

	A_1	A_2	A_3	b_1	b_2	T_1	T_2	T_3
Original LB	0.3	0.7	-	0.14	0.53	-	-	-
3G LB	0.165	0.335	0.5	-	-	20	4.5	$1.25M$

Table 2.1: Empiric coefficients independent from Mach number and profile

- $\mathbf{T_{p,b,f,v,VL}}, \eta$: These constants are also found empirically but differ from the latter by their dependence on the Mach number and sometimes even on the aerodynamic profile. Because the Mach number is very low in the context of VAWTs, the values gathered here are often taken from a Mach number $M = 0.3$. The following table provides an overview of the constants from the different sources :

	T_p	T_b	T_f	T_v	T_{VL}	η
Original LB - Dyachuk [13]	1.7	-	3	6	7	0.95
3G LB - Dyachuk [13]	1.7	-	3	10	8	0.95
Scheurich [30]	1.7	4	3	6	7	0.95
VPM [23]	1.7	4	3	6	7	1
Balbino [2]	1.5	-	5	6	5	0.95
Beaudet [6]	1.7	3.93	3	6	7.5	0.95
Chantharasenawong [5]	1.7	-	3	6	7	0.97
Present work	1.7	4	3	6	7	1

Table 2.2: Empiric coefficients independent from Mach number and profile

There is quite a consensus for the values of T_p and T_f that were respectively taken equal to 1.7 and 3. Regarding the values T_b, T_v and T_{VL}, they come from modifications of the 3G model that are not present in all the previous works and that were taken from [23]. Therefore, following the values of [23] seems the most appropriate. At last, the value of $\eta = 1$ was chosen because it allows to better fit the static airfoil data [23].

Chapter 3

Implementing the dynamic stall

In this chapter, more light is shed on the concrete implementation of the dynamic stall in actuator line model and actuator cylinder model codes. To this end the flow solver developed at UCLouvain, BigFlow, is first briefly presented. Then, the actuator line model is described and the implementation of the dynamic stall in this existing code is explained. Following the same reasoning, the ACM is detailed as well as the implementation of the dynamic stall in this existing code, also developed at UCLouvain (see [37]).

3.1 Flow solver

The flow solver used in this work to perform LES of turbulent incompressible flows is called BigFlow and has been developed by Duponcheel [12] at UCLouvain based on previous works (Bricteux, Georges). The explanations on this flow solver are coming from [12], [34], [26] and [25].

The goal of this flow solver is to solve the Navier-Stokes equations supplemented by a sub-grid scale model :

$$\nabla \cdot \mathbf{u} = 0 \tag{3.1}$$

$$\frac{\partial \mathbf{u}}{\partial t} + (\mathbf{u} \cdot \nabla)\mathbf{u} = -\nabla P + \nabla \cdot (\tau + \tau^{sgs}) + \mathbf{f} \tag{3.2}$$

where $P = \frac{p}{\rho}$, $\mathbf{f}$ represents the external forces, τ is the shear stress, and τ^{sgs} stands for the artificial shear stress added to model the turbulence of the sub-grid scales. The latter is computed using either a classical Smagorinsky model or a a Regularized Variational Mustiscale model (see [12]) depending on the presence of a wall model.

The equations are discretized using the primitive variables (i.e. velocity and pressure) on a structured staggered mesh. A fractional step method is used with the "delta-form" for the pressure (see Lee *et al.* [18]), i.e. the pressure serves to compute the predictor field and a Poisson equation only arises in the computation of the pressure difference. This fractional step strategy is second-order accurate in time [18].

The equations are discretized in space thanks to a fourth-order finite difference scheme and integrated in time using a second-order explicit Adams-Bashfort scheme. Three layers of ghost points are then necessary to ensure the fourth-order accuracy. Dirichlet and Neumann conditions are possible, conversely to an unbounded flow [34].

The Poisson equation, which is the most consuming step, is solved through a multigrid solver with a Gauss-Seidel smoother. The idea of a multigrid solver is to accelerate the convergence by solving the problem on different grid levels, thus reducing the range of error frequency related to the size of the different grids. This Poisson solver has been designed in order to perform efficiently during parallel simulations, i.e. the processors are allowed to agglomerate to form a coarser grid.[12]

3.2 Actuator line

3.2.1 Theoretical background

Before the implementation of the dynamic stall is explained, some theoretical background on the ALM is provided. The information on this method is mainly coming from [34], [24] and [1].

In an ALM, the blades of the VAWT are replaced by lines of control points located at their quarter-chord, as depicted on figure 3.1. These actuator lines are rotating as does the VAWT. After an interpolation of the velocities is carried, the blade element theory is applied to compute the forces and at last, the forces are distributed on adjacent grid points.

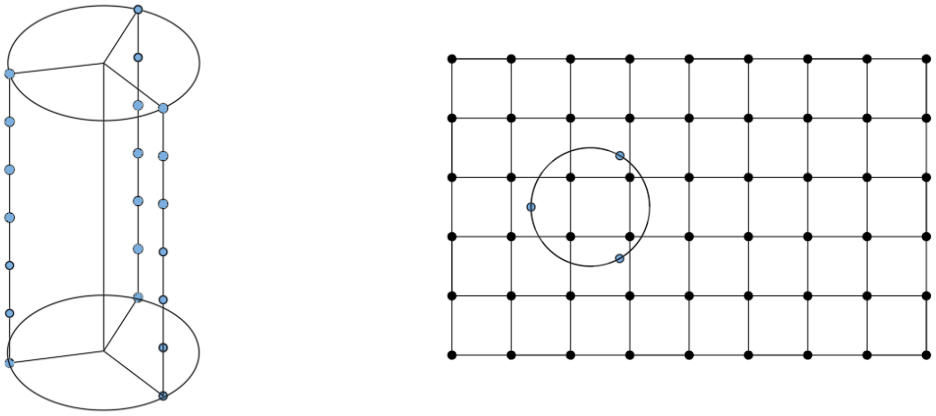

Figure 3.1: Actuator line model

The first step of an ALM is to interpolate the velocities of the flow computed by the flow solver on the control points of the actuator lines. Indeed, as shown by figure 3.1, the control points of the lines do not necessarily coincide with grid points. This interpolation is done here with a M_4' kernel, an isotropic interpolating function (see Monaghan [28] for more information), but the interpolation could be done using others schemes (see [34] for more information). The M_4' method uses a cube made of 64

mesh points around the line point to interpolate the velocities on the latter [37]. The interpolation thus reads :

$$u_j = \sum_{i=0}^{64} u_i \, W(\frac{x_j - x_i}{h}) W(\frac{y_j - y_i}{h}) W(\frac{z_j - z_i}{h}) \tag{3.3}$$

where the indexes j refer to an actuator line point whereas the indexes i refer to a mesh point. $W(x)$ is the M_4' interpolation kernel given by [36]:

$$W(x) = \begin{cases} 1 - \frac{5}{2}|x|^2 + \frac{3}{2}|x|^3 & if \ \ |x| < 1 \\ \frac{1}{2}(2 - |x|)^2(1 - |x|) & if \ \ 1 < |x| < 2 \\ 0 & if \ \ |x| > 2 \end{cases} \tag{3.4}$$

This weight function allows the mesh points closer to the line point to be preponderant.

Once the velocities at the lines points are evaluated, the blade element theory is used to compute the forces. For the following, it is important to bear in mind section 2.3.1 and figure 2.2 where some important parameters are defined.

Using their definition, the lift and drag forces per unit span can be derived :

$$L = \frac{1}{2}\rho \|\overrightarrow{W}\|^2 c \, C_l(\alpha) \tag{3.5}$$

$$D = \frac{1}{2}\rho \|\overrightarrow{W}\|^2 c \, C_d(\alpha) \tag{3.6}$$

where the lift and drag coefficients emanate from the static polar data.

The reaction of the forces produced by the flow on the blades now have to be applied on the flow. To this end, the first step is to express these reaction forces in the coordinates system (x, y, z) of the flow. Trivial trigonometry relations provide N and T (also called F_n and F_t in some references) from L and D as well as F_x and F_z; one obtains :

$$F_x = N \cos\theta + T \sin\theta \tag{3.7}$$

$$F_z = -N \sin\theta + T \cos\theta \tag{3.8}$$

These forces are then added as a body force in the Navier-Stokes equations [1]. Furthermore, the flow solver takes external body force per volume and so F_x and F_z, which are per height unit here, have to be multiplied by $\frac{dh}{dxdydz}$, where dh is the space between two control points on the actuator line and dx, dy and dz represent the size of a grid cell of the mesh [37].

At last, following the opposite reasoning than before, these forces have to be applied on the numerical implementation of the flow. This is done with a 2D gaussian kernel

spreading the forces perpendicular to the span of the blades in the case of the ALM. The 2D gaussian weight function is defined as follows :

$$W(x) = \frac{1}{\pi\sigma^2} \exp\left(-\frac{d_c^2}{\sigma_c^2}\right) \exp\left(-\frac{d_t^2}{\sigma_t^2}\right) \tag{3.9}$$

where σ_c and σ_t respectively represent the standard deviations in the chord and thickness directions and d_c and d_t stand for the distances between the actuator line point and the mesh point in the chord and thickness directions. The 2D gaussian was observed to perform better than a more versatile and classical distribution like $M4$ for the actuator lines as it handles the tip-blade behaviour of the VAWT better, without adding non-physical forces in the blade direction. [34]

3.2.2 Implementation of the dynamic stall

As the LB model of the dynamic stall changes the force coefficients C_n and C_t, it has to be included in the second part of the ALM, i.e. in the computations of the blade forces exerted on the flow.

Introducing the dynamic stall in an ALM code is by far easier than in an ACM code. Indeed, the locations of the actuator lines are evolving in space and the code computes each control point at each time step. Therefore, it is sufficient to store or update the values to handle the fact that the LB model refers to the previous time step. Once the force coefficients have been updated with the adding of the dynamic stall, the flow will naturally update itself thanks to the distribution forces kernel. The dynamic stall does not modify the first and third steps of the actuator lines method, i.e. the interpolation of velocities on the control points and the force distributions on grid points.

Since ALM (or ACM) is a model that completely solves the flow, the deficiency functions 2.29 on the angle of attack should not be implemented. Indeed, the equivalent angle of attack is directly provided by the code, conversely to methods that are not solving the flow, like the DMST for example.

All the deficiency functions, which are used here to induce delays, are initialized to 0 in the code. These initializations are allowed because the airfoil is stationary until the computations begin [5].

As written in part 2.3.2.1, the impulsive component of the unsteady attached flow normal force coefficient is extremely small, to the extent that it can be neglected without consequences[6]. This component was thus not implemented in the code.

3.3 Actuator cylinder

3.3.1 Theoretical background

The actuator cylinder method is highly related to the actuator lines one. The three main steps stay the same but the real change remains in the position of the control points. Whereas the control points in an ALM are located only on lines at the position of the blades (which thus evolve with time), the control points in an ACM are distributed

along the cylinder that represents the external surface of the VAWT, as shown in figure 3.2. The blades are thus not effectively represented in this method and they are replaced by an actuator surface corresponding to an infinity of blades. [37], [16]

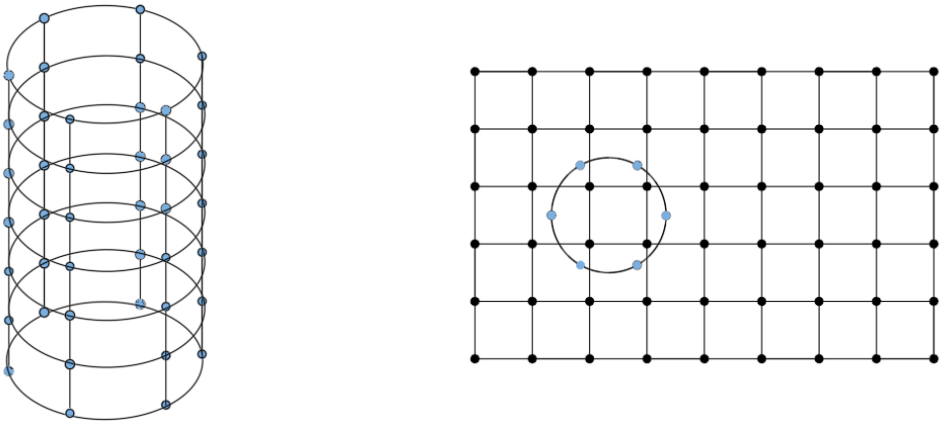

Figure 3.2: Actuator cylinder method

Regarding the implementation, the explanations of section 3.2 apply here as well and what is done for a control point of an actuator line is also done for a control point of an actuator cylinder. One of the differences is that the forces that have to be applied on the flow should be divided by the number of points along the perimeter of the cylinder N_θ to account for the fact that there is only a finite number of blades. Also, the forces distribution kernel is different from the one in an ALM; an $M4$ scheme is used here :

$$F_i = F_j \, W(\frac{x_i - x_j}{h}) W(\frac{y_i - y_j}{h}) W(\frac{z_i - z_j}{h}) \tag{3.10}$$

where the meanings of i, j and $W(x)$ have not been changed compared to the $M'4$ scheme developed above.

3.3.2 Implementation of the dynamic stall

Implementing the Leishman-Beddoes model of the dynamic stall on an actuator cylinder model is more complex than on an actuator line model.

Since the effect of the blades is distributed all over the cylinder, space and time merge. Where some parameters are taken at the previous time step in an ALM, some parameters are taken on the same ring of control points but at the previous points spatially in an ACM. This implies that iterations on each ring of control points have to be done because the first control point is taking data that has not been updated yet. For more clarity, it is worth taking a look at figure 3.3, representing a ring of control points on an actuator cylinder. The green points represent the points that are already updated while the red ones illustrate the points that still have to be updated. For the first point, taking the data from the previous time step - as it is needed in the LB model - is equivalent in ACM to taking the data of the last point, i.e. at point 8 on the figure. However, this data has not been updated yet and the new parameters of point 1 are

then inaccurate. The situation improves when the code goes to the other points, but as the first point is inaccurate, by definition, all the other points will not be perfectly correct.

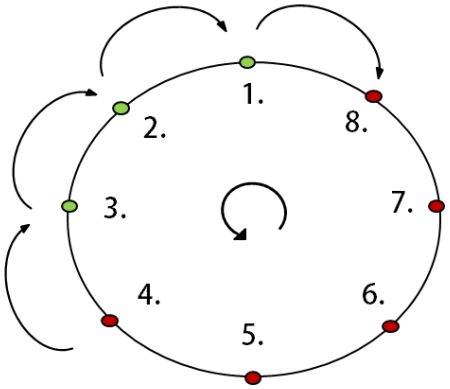

Figure 3.3: Convergence issue Dynamic Stall ACM

Therefore, multiple iterations have to be processed on each ring of points of the actuator cylinder in order to smooth out these errors. A convergence analysis was carried out to this end, where the error E on one ring of control points was defined as the sum of the differences in terms of normal force coefficient at each control point between two iterations :

$$E = \sum_{i=0}^{N_\theta} |C_{n_{k,i}} - C_{n_{k-1,i}}| \tag{3.11}$$

where N_θ is the number of control points on a ring. This error E appears to be pretty close to zero after a maximum of 3 iterations i.e. E is lower than 10^{-10} within 3 iterations in any case. The threshold used in the code is the following : when the error E becomes lower than 0.1, the code proceeds to a last iteration. Thus, the data of all the control points are written in the output file only during this last iteration and do not have to be continuously stored. Empirical testings have shown that the convergence is extremely quick and if E is already lower than 0.1, adding an iteration pushes the error E to values ridiculously close to 0.

In order to limit the error E, the starting point of the process was set at an angle $\theta = 90°$ (see figure 3.3). Indeed, the flow is supposed to be attached at this position and therefore the error between two time steps should not be too large. Experience has shown that doing this allows to save up to one iteration compared to situations where the reference starting point is located right in the dynamic stall process.

Once this ACM-related particularity of convergence has been overcome, the rest of the implementation follows the one of an ALM : the model is applied on the force coefficients, the deficiency functions do not need to be taken into account in the computation of the equivalent angle of attack, the other deficiency functions are initially set to 0 and the impulsive component of the unsteady attached flow part $C^I_{n_k}$ is neglected.

Chapter 4

Results

In this chapter,VAWTs are simulated using both the ALM and ACM with the dynamic stall model. Firstly, a validation of the model is carried out on a simple pitching blade. Secondly, the set-up of the VAWT simulations is explained and justified. Thirdly, a transverse comparison between the ALM, the ACM, a VPM method and a DMST is done with the dynamic stall model used in the code of VPM. This is realized for various TSRs. Fourthly, a comparison between the ALM and the ACM is done with the refined model, including the improvements from section 2.3.4. At last, conversely to all the previous results, simulations are done for ALM and ACM with a turbulent inflow. Again, the wakes and force curves are compared and analyzed.

4.1 Validation

Before applying the dynamic stall model to complete VAWT simulations, a validation must be carried on a more simple case. As it was done in [30] and [23], the model is then applied on a simple pitching blade oscillating following a VAWT function. The results obtained are then compared to the results of the VPM simulations coming from [23].

4.1.1 Practical frame

The simulations on a pitching blade are carried out in pseudo 2D, which requires some adaptations. Among others, in order to avoid a decay of the normal velocity when the drag coefficient is high, the velocities are imposed using the upstream velocity U_∞. As a consequence, the equivalent angle of attack becomes equal to the geometric angle of attack artificially provided to the code. This assumption is realistic if the figure 4.1 showing the differences between the dynamic equivalent angle of attack, the static equivalent angle of attack and the geometric angle of attack is observed [23]. One finally gets an infinite aspect ratio 2D VAWT with one blade and no rotation.

The pitching effect is obtained using a geometric angle of attack that reproduces the changes in angle of attack undergone by a VAWT blade. This geometric angle of attack, defined by [30], is only function of the TSR λ and the azimuthal position or, equivalently, the product of the angular speed ω and the time t :

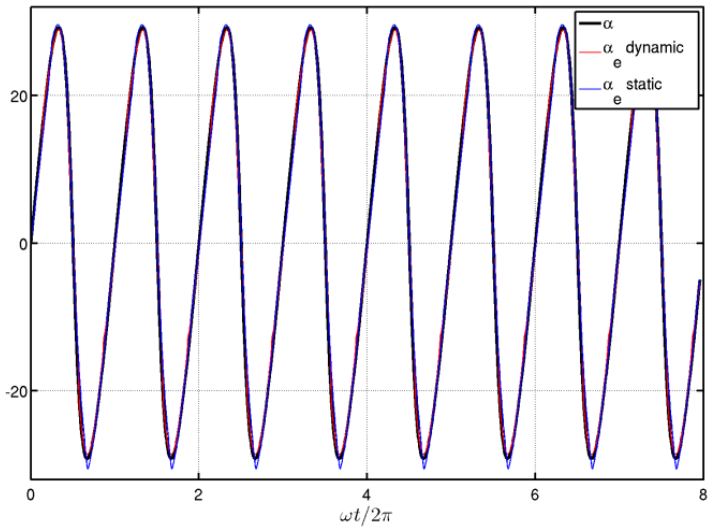

Figure 4.1: Comparison between dynamic equivalent angle of attack, static equivalent angle of attack and geometric angle of attack[23]

$$\alpha = \arctan\left(\frac{\sin\omega t}{\lambda + \cos\omega t}\right) \tag{4.1}$$

The TSR is taken equal to 2.05 here and the reduced frequency k to 0.05 in order to be consistent with the VPM validation test to which the present simulation is compared. Therefore, the following constants are defined : $U_\infty = 1[\frac{m}{s}]$, $\omega = 0.1[\frac{rad}{s}]$ and $c = 1[m]$. As mentioned in the introduction, the reduced frequency expresses the unsteadiness of the flow and a value of 0.05 is often taken to see the effects of unsteadiness appear [6]. The geometric angle of attack thus defined can be seen on figure 4.1.

In order to make a fair comparison with the VPM validation model, the same model of dynamic stall and same constants were used. The model used by VPM is the third-generation Leishman-Beddoes model without the last two improvements of section 2.3.4 i.e. the differentiation of the tangential and normal separation points is not implemented and the model of Urbina to allow the tangential force coefficient to get negative values is replaced by the subtraction of a constant K. The resulting force coefficients of the model as implemented in the VPM simulations [23] are therefore the following :

$$C_n = C_{n\alpha} \cdot \sin\alpha \cdot \left(\frac{1+\sqrt{f_k}}{2}\right)^2 \tag{4.2}$$

$$C_t = \eta \cdot C_{n\alpha} \cdot \sin\alpha \cdot \alpha \cdot \left(\sqrt{f_k''} - K\right) \tag{4.3}$$

The same static constants as in VPM simulation were also used and these constants are coming from [30]. These are derived from polars of a NACA0015 airfoil at a Reynolds number of 800000 and are summarized in table 4.1. The empirical coefficients can be found in table 2.2 at the line VPM.

C_{n_α}	α_1	K	S_1	S_2	C_{n_1}
5.73	14°	0.23	0.06981	0.03054	1.294

Table 4.1: Coefficients used by the VPM simulation, derived from a NACA0015 airfoil at a Re = 800000 [30]

4.1.2 Results of the validation

The results of the validation are presented on figures 4.2 and 4.3. The blue curves represent the simulations done in this work using the pseudo 2D with BigFlow whereas the red curves depict the reference VPM simulation. Black dotted curves characterizing the static behaviour (thus without the implementation of the dynamic stall) are also shown on these figures. All the force coefficients C_l, C_d, C_n and C_t are expressed in function of the angle of attack.

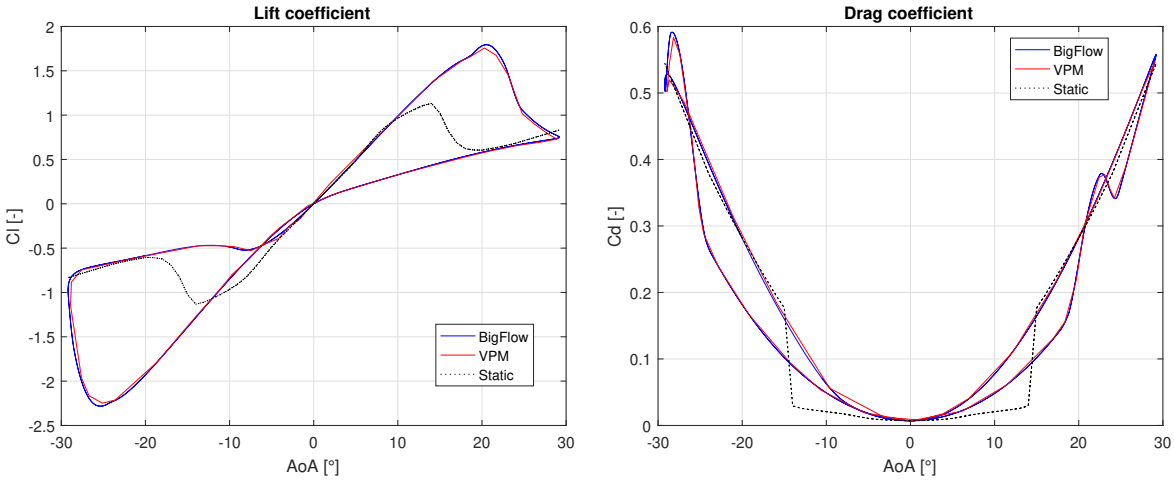

Figure 4.2: Lift and drag force coefficients of the pitching blade

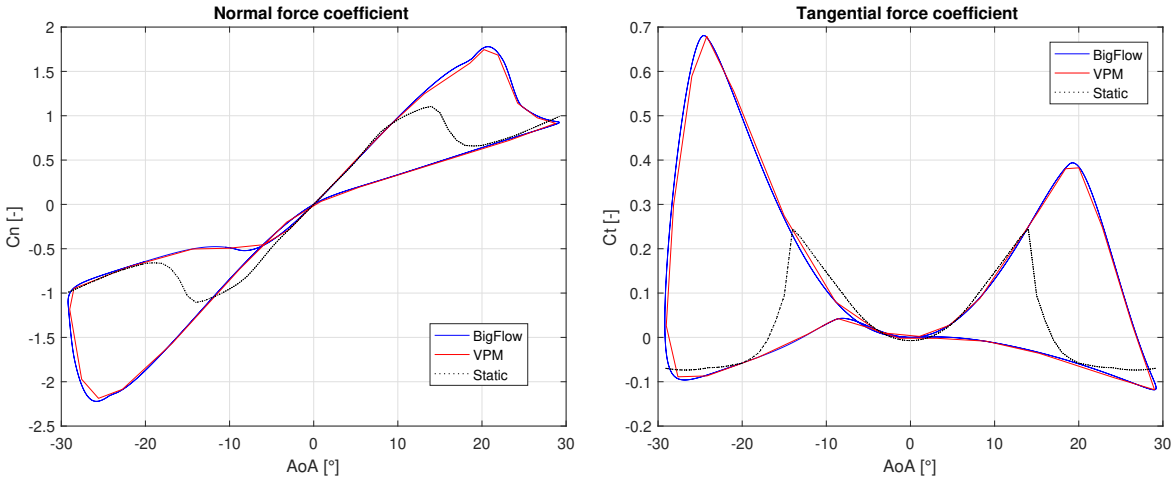

Figure 4.3: Normal and tangential force coefficients of the pitching blade

Two main considerations emanate from these results :

- The dynamic stall model implemented on BigFlow can be validated and further be used on more complex and complete architectures like the modelisation of VAWTs through the ALM and the ACM.
- As explained in chapter 2, the force coefficient curves with the dynamic stall tend to follow the behaviour of the static curves quite well until the static stall angle of attack of 14° is reached. After that, the dynamic stall indeed provides an increment of lift followed by a severe stall and values that stay well below the static ones until the reattachement of the flow.

4.2 Numerical simulation of VAWT

A lot of parameters are involved in the numerical simulation of a VAWT. This section aims to define them as well as to justify the choices made. For the following, x represents the streamwise direction, y the vertical direction and z the spanwise direction.

4.2.1 Wind turbine

The characteristics of the studied wind turbine are summarized in table 4.2. The airfoil shape of the wind turbine blades is the NACA0015 profile. The following data were chosen because they are similar to the data used in the VPM and DMST results, which are compared to the present simulations in the following section.

The simulations are processed at three different rotational speeds : 150, 225 and 300 $[rpm]$. Taking into account that the upstream velocity is set at 11 $[\frac{m}{s}]$, the three working TSR are 2.14, 3.21 and 4.28.

Rotor height H	4.5 [m]
Rotor radius R	1.5 [m]
Blade chord c	0.1725 [m]
Aspect ratio AR	1.5 [-]
Number of blades	3 [-]

Table 4.2: Characteristics of the studied VAWT

4.2.2 Domain size and boundary conditions

The domain is a rectangular parallelepiped outspread in the streamwise direction x. Doing this and locating the VAWT at the beginning of the domain allows to have a view on the wake of the VAWT. The length of the domain was chosen to be 48 [m] or 16 diameters because this length is sufficient to be able to analyze the wake, as shown in section 4.3.

Regarding the vertical direction y and the spanwise direction z, an analysis was carried out in order to quantify the blockage effect. For this purpose, different simulations of ACM are launched and different possibilities for both the width and the height of the domain are explored : 18, 30, 36 and 48 meters, or equivalently 6, 10, 12 or 16 D. To know which sizes are the most suitable, the power coefficient C_P [1] is plotted in function of the time and the simulation that exhibits a reasonable converged C_P is conserved. The results can be observed on figure 4.4. The size of $10D$ was retained for the y and z directions as they prove to make the C_P converging without being too large and thus providing a more lightweight computational cost.

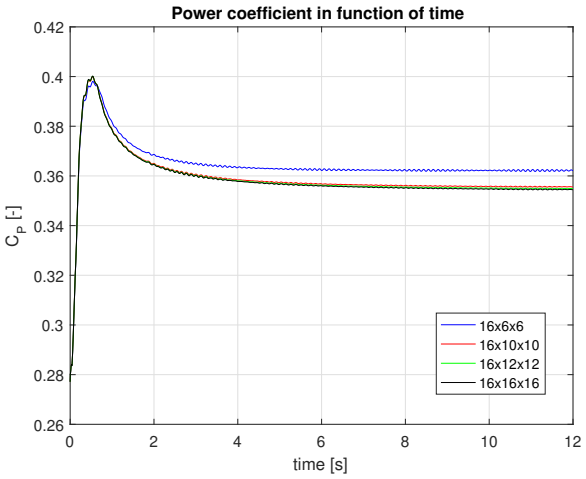

Figure 4.4: Analysis of the domain size in the directions y and z

In the x direction, the velocities are fixed at the inlet of the domain, at 11 $[\frac{m}{s}]$ and a convective boundary condition is imposed at the outlet. No-through conditions are enforced in the y direction. At last, periodic boundary conditions are set in the z direction.

4.2.3 VAWT location

The VAWT is centred in the y and z directions and located in an advanced x position i.e. it is located at a position ($3D$, $5D$, $5D$), as shown in figure 4.5.

The reference for the azimuthal position is placed at an angle of 90° on the classical trigonometric circle. As explained in section 3.3.2, locating the zero of the azimuthal position at the beginning of the upstream part[2] of the rotor allows to avoid some extra iterations in the case of the ACM.

[1] The power coefficient C_P is obtained by adimentionalizing the mechanical power as following : $C_P = \frac{P_{mec}}{0.5\,AR\,\rho\,U_\infty^3}$

[2] The upstream part corresponds to [90°, 270°] on the trigonometric circle, the downstream one corresponds to the other half-circle.

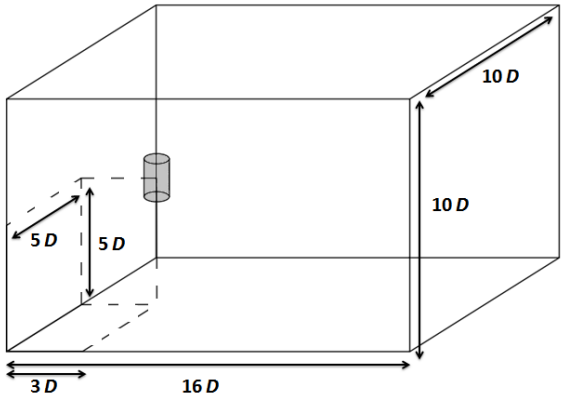

Figure 4.5: Location of the VAWT in the domain

4.2.4 Blade resolution

In the frame of an ACM simulation, the number of control points on the VAWT in the vertical direction was also subject to C_P convergence analysis. The result is shown on figure 4.6. It can be seen that the influence of the number of control points along the blade N_r is limited. However, it was chosen to take $N_r = 48$ as it is more accurate and does not generate huge simulation costs.

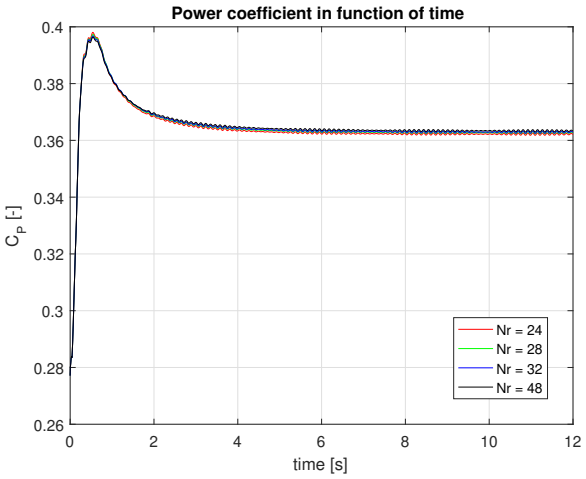

Figure 4.6: Analysis of the blade resolution

4.2.5 Domain resolution

The domain resolution is expressed in number of grid points by diameter. It has to be such that elements of the blade are larger or equal to the BigFlow spatial discretization. Therefore, the resolution was chosen to be 32 grid points by diameter in the three directions, which results in a number of grid points on the blades that is equal to the number of control points. This resolution is already quite fine and heavy; the number of grid points is superior to $52 \cdot 10^6$. Upgrading to 48 points by diameter would have brought enormous computational costs.

However, the simulations of section 4.5 including the turbulence show to already have a repulsive cost by their turbulent nature. Therefore, these simulations were done on a resolution of 32 grid points in the vertical direction while only 16 grid points were put in the spanwise and streamwise directions. Doing this maintains a sufficient number of grid points on the blade to capture the force variation on it. It can be seen on figure 4.7 that this gives a little less accurate results; but still better than a resolution of 16 points per diameter in each direction.

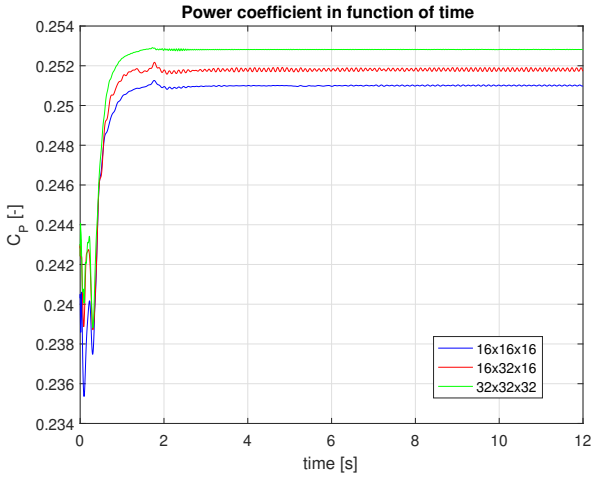

Figure 4.7: Analysis of the mesh resolution

4.2.6 Time step

The time step has to be chosen such that the CFL constraint is satisfied. In BigFlow, it has to be less than 0.2 and is taken less than 0.15 by considering a security margin :

$$CFL = \frac{U_\infty \Delta t}{\Delta x} < 0.15 \tag{4.4}$$

Provided that U_∞ was fixed to 11 $[\frac{m}{s}]$ and Δx is worth $0.09375[m]$, the maximal time step is 0.00127 $[s]$.

Furthermore, for the ALM, one must avoid that the blade crosses more than one mesh grid size in less than one time step. Inserting a security margin, this constraint translates to :

$$\frac{\omega R \Delta t}{\Delta x} < 0.5 \tag{4.5}$$

Wrapping these two constraints up, a time step $\Delta t = 0.001[s]$ works for both ALM and ACM simulations in the established conditions.

4.2.7 Simulation time

The simulations are carried out on 3 convective times (equal to 13091 Δt), so that the wake has the opportunity to develop and the C_P is by far converged. When statistics are done on the wake (see sections 4.3 and 4.5), the data are gathered on the second 1.5 convective time. The first 1.5 convective time is kept to let the wake develop itself.

The force curves or force coefficients are averages of data gathered during 5 revolutions of the VAWT (this corresponds to between 1000 Δt and 2000 Δt, depending on the TSR).

4.3 Results using VPM constants

In order to make fair comparisons with the VPM reference, simulations with the ALM and the ACM were carried out using the same implementation of the dynamic stall, as well as the same constants as in the VPM simulations (see section 4.1.1 and table 4.1 for more details on the VPM choices).

Some of the results of the ALM and the ACM are also compared with the DMST simulations provided by Gauthier Georis from WaPT [38]. These DMST simulations were also carried out using the VPM dynamic stall model and constants. The expansion of the streamtubes was implemented here to be more realistic and to respect the mass flow conservation.

4.3.1 Force curves

Figure 4.8 presents the evolution of the angle of attack α in function of the azimuthal position θ for the three studied TSR. These curves are helpful to improve the understanding of the following results and globally follow the behaviour of the static curves. The flattening of the angle of attack in the downstream part of the rotor when the TSR increases is due to the fact that the load on the wind turbine is more important (see forces curves 4.9, 4.10 and 4.11) resulting in a slower flow. Some oscillations are present for the ALM when the blades start to hit their wake ($\theta \approx 200°$). It can also be observed that the DMST results underestimate the absolute value of the angle of attack, no matter the TSR. However, as these simulations were not done with a flow solver, they are less accurate.

The normal and tangential force curves for the three TSR are depicted on figure 4.9, 4.10 and 4.11 . They are adimensionalized by a factor cq_0 where $q_0 = 0.5U_\infty\rho$.

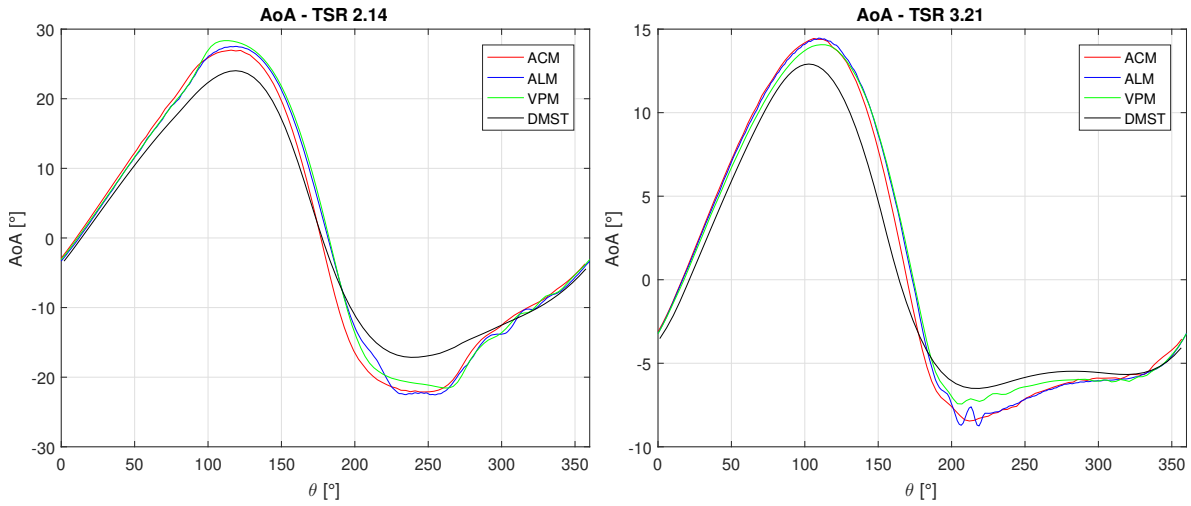

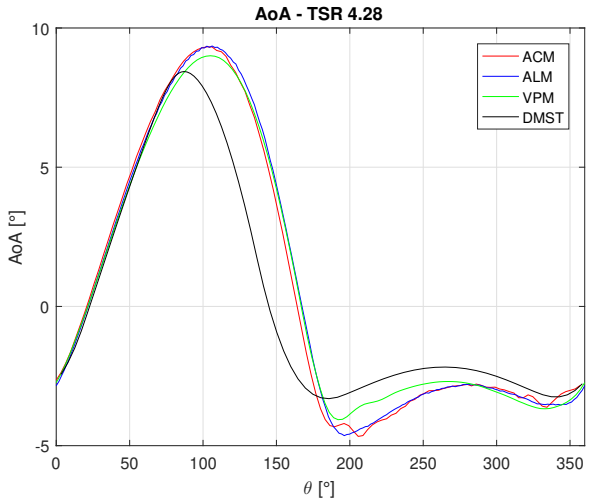

Figure 4.8: Angle of attack in function of azimuthal position θ

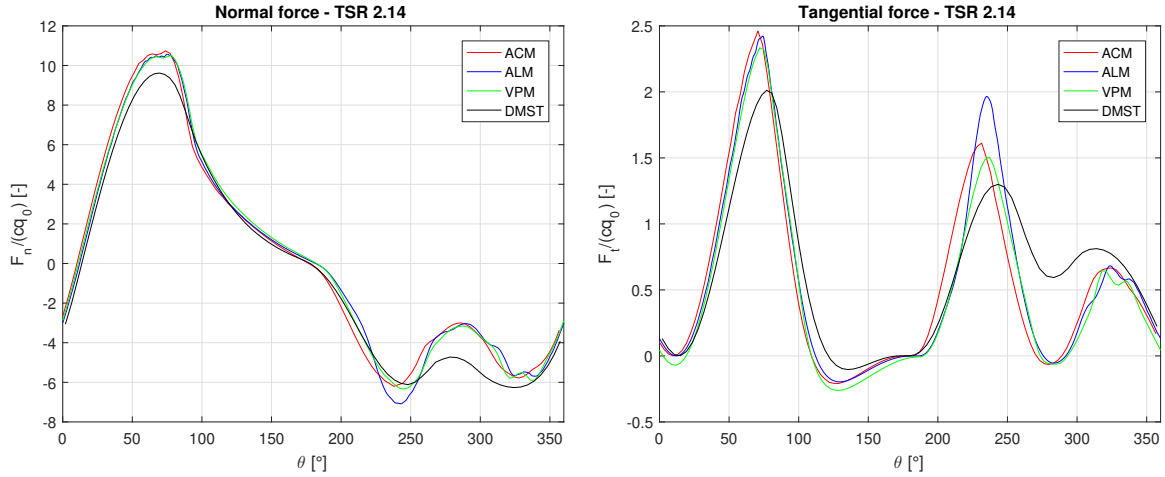

Figure 4.9: Normal and tangential forces in function of θ for TSR 2.14

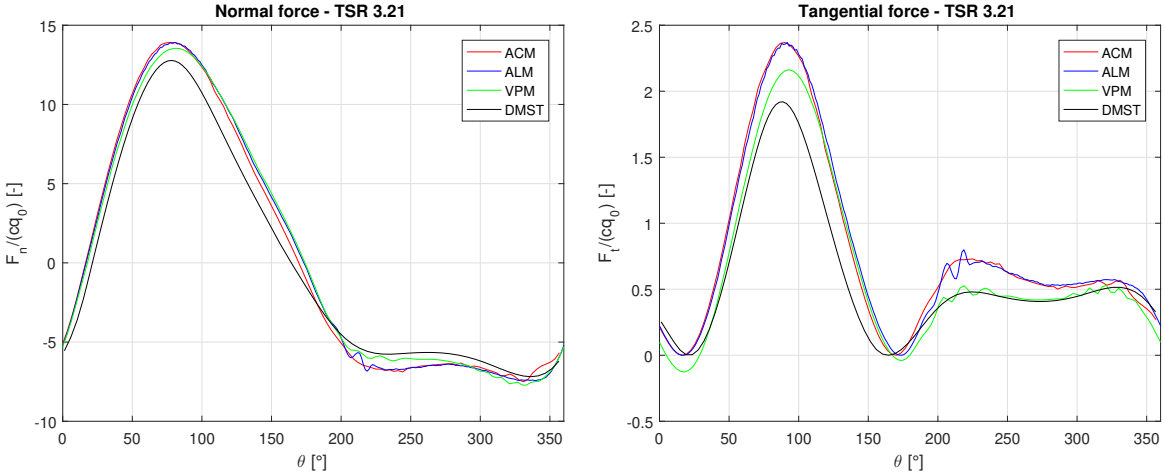

Figure 4.10: Normal and tangential forces in function of θ for TSR 3.21

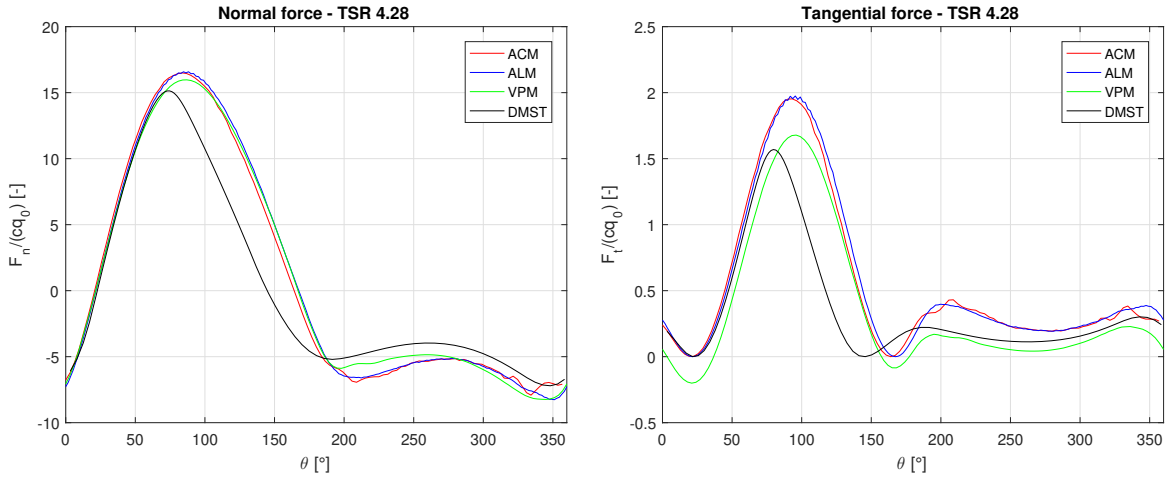

Figure 4.11: Normal and tangential forces in function of θ for TSR 4.28

Different observations emanate from these graphs :

- The ALM and the ACM show almost perfect agreement with VPM regarding the normal force.
- Oscillations near $\theta = 200°$ for the ALM at the TSR 3.21 originate from the oscillations in the angle of attack.
- The ALM and the ACM show tendencies to overestimate the tangential force, especially for high TSR. These differences also arise if the unsteady effects are ignored; the effects of dynamic stall indeed vanish in case of high TSR because the static stall angle of attack is never reached. The differences between ACM and VPM at high TSR can be retrieved in [37].
- The ALM and ACM show almost perfect agreement between each other except for the TSR 2.14 where the ALM exhibits higher tangential and normal peak forces in the downstream part of the rotor. This difference is due to the fact that the velocity fields differ between ALM and ACM, as it is shown below. The averaged streamwise velocity fields are shown in section 4.3.3 and the instantaneous ones are present in appendix A.
- The descending part of the two peaks of the tangential force for the TSR 2.14 correspond to the stall of the VAWT : the first decrease corresponds to the ejection of the dynamic stall from the blade in the upstream part of the rotor, the latter corresponds to the same ejection in the downstream part of the rotor. The first peak reaches a higher value than the second one as the kinetic energy present in the flow is reduced after it has encountered the blade for the first time.
- The results of the DMST are shown here for completeness sake but will not be shown anymore in the rest of this work as they step aside from the initial objectives and show not to be so accurate. However, the general behaviour is always respected. Indeed, as the DMST underestimates the angle of attack, it also underestimates the forces. Furthermore, the expansion modelled in the DMST simulations is overestimated, which leads to a power deficit [9].

Next, the curves for the force coefficients C_n, C_t, C_l and C_d for the three working TSR are shown on figures 4.12, 4.13 and 4.14.

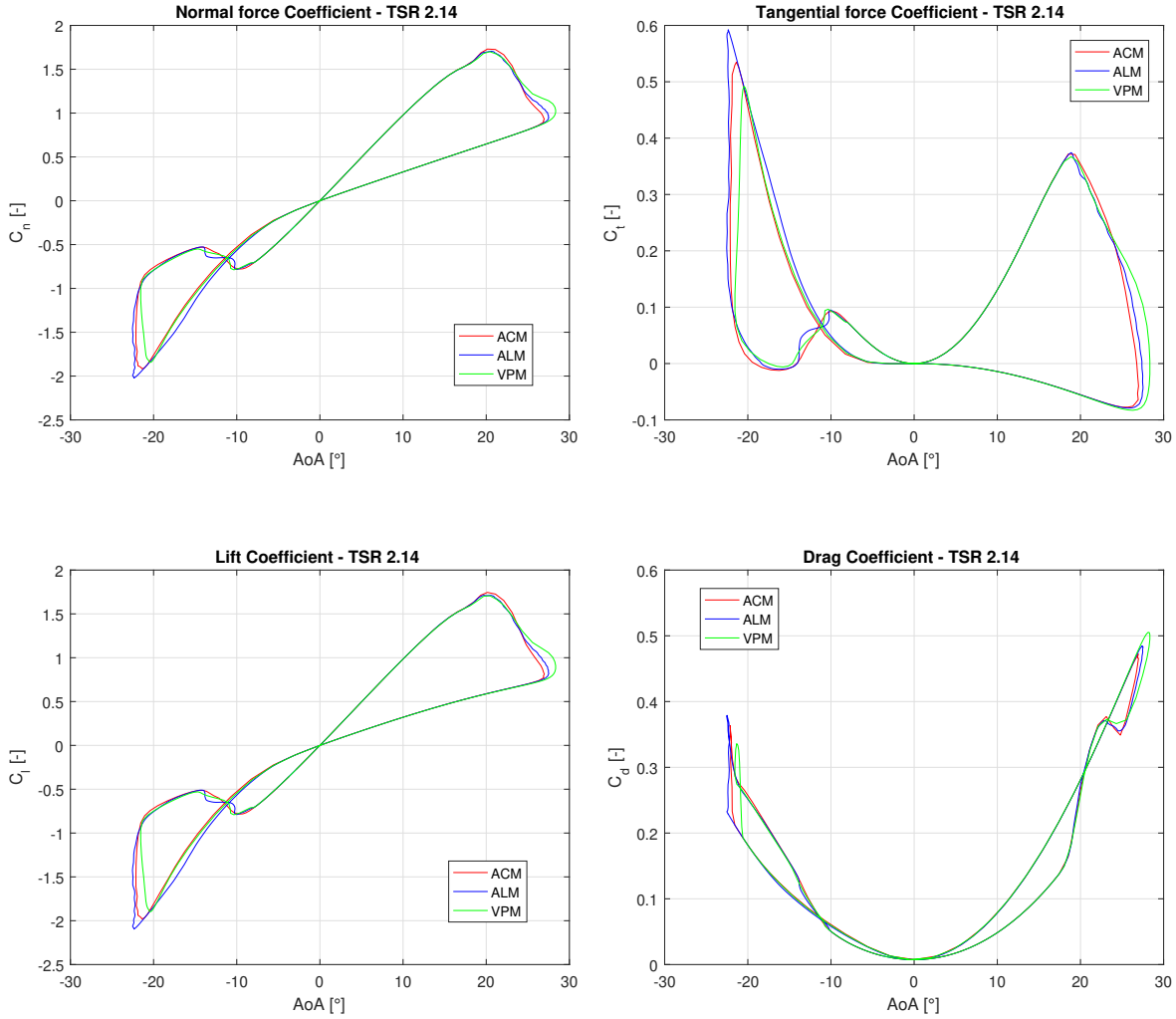

Figure 4.12: Normal, tangential, lift and drag force coefficients in function of the angle of attack for TSR 2.14

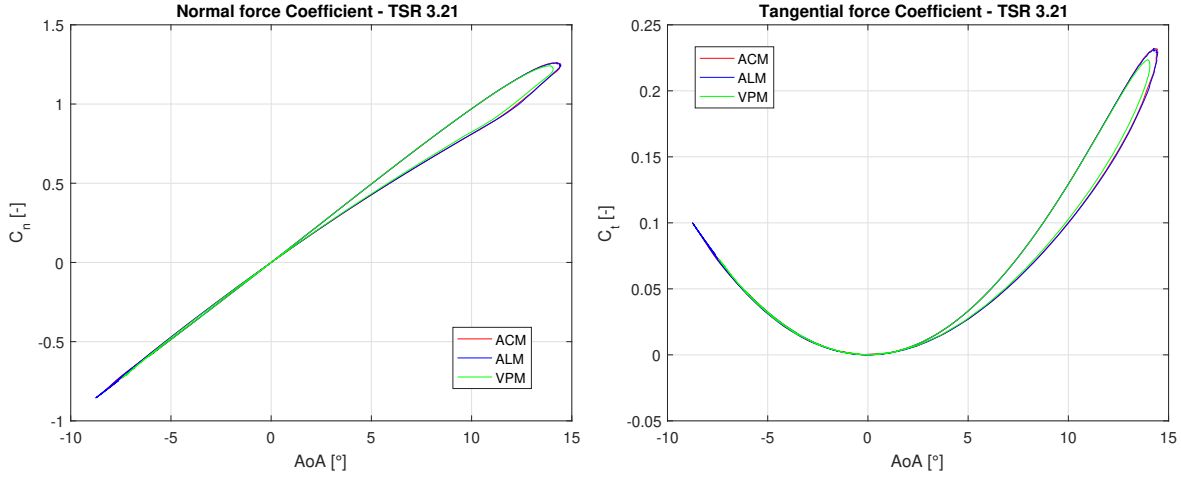

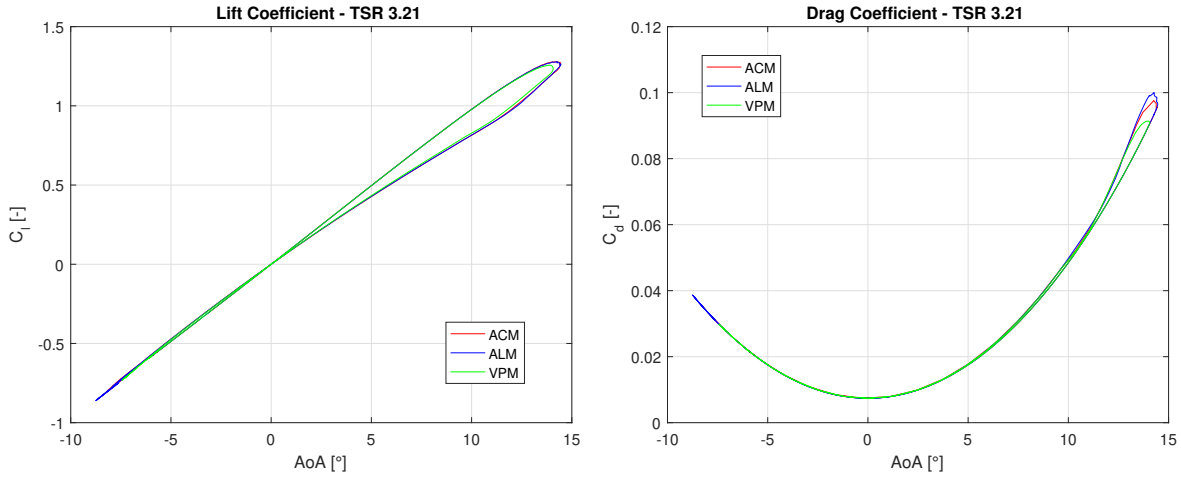

Figure 4.13: Normal, tangential, lift and drag force coefficients in function of the angle of attack for TSR 3.21

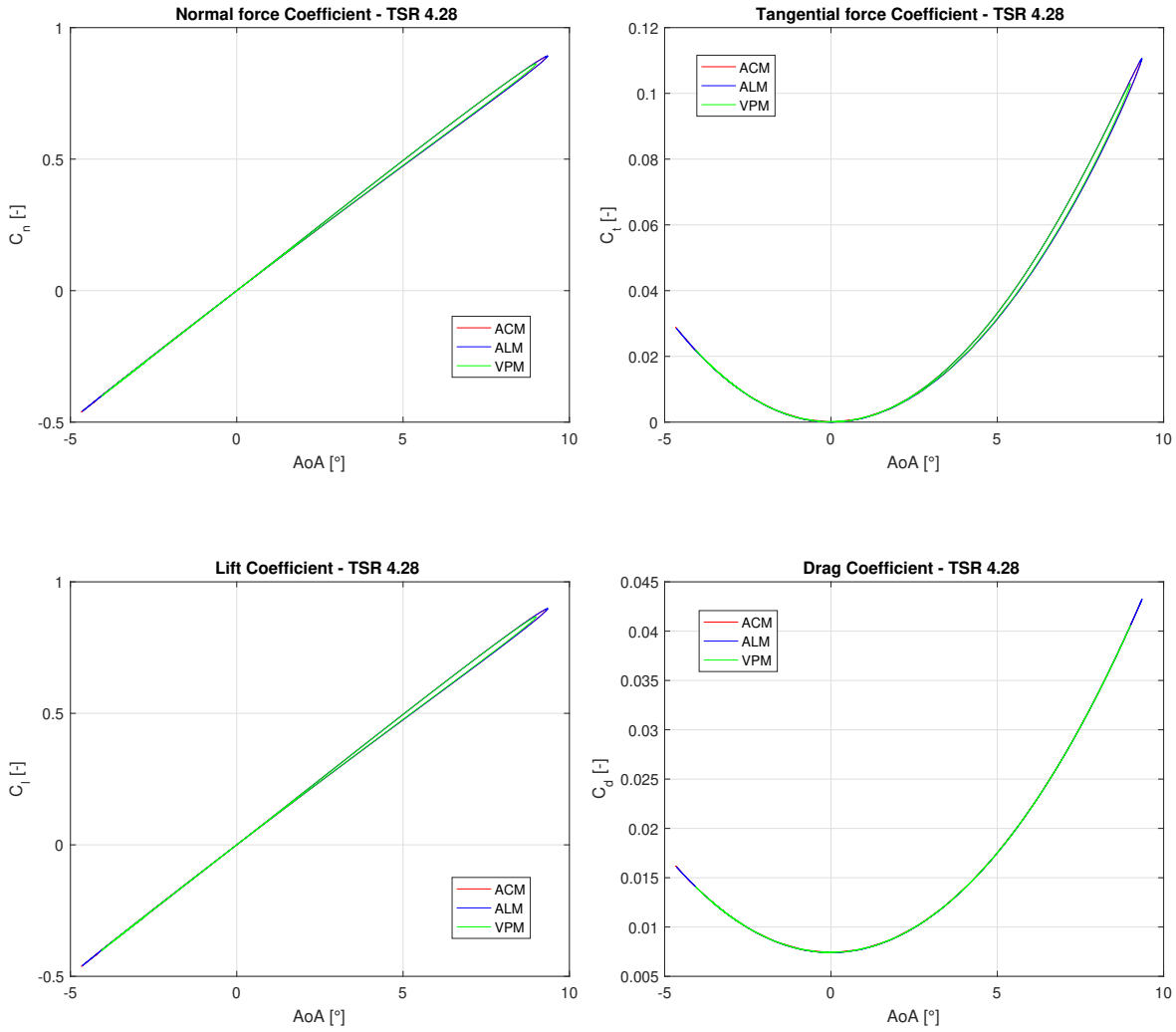

Figure 4.14: Normal, tangential, lift and drag force coefficients in function of the angle of attack for TSR 4.28

Firstly, without any surprise as it was already the case for the force curves, the ALM and ACM provide good results compared to the VPM simulations. The three models exhibit the same behaviour and only small differences that concord with the previous observation of the force curves arise.

Then, as it was already mentioned, the dynamic stall effects are unimportant at high TSR : they are barely visible for the TSR 3.21 and totally absent for the TSR 4.28. As a consequence, the focus will be put on the TSR 2.14 and sections 4.4 and 4.5 are only centered on this TSR. For the TSR 4.28, the lift and drag curves refer to the static polar of Reynolds 800000 when the flow is still attached. Indeed, the curve of the angle of attack for the TSR 4.28 (see figure 4.8) proves to never pass the static stall angle of attack.

Regarding the TSR 2.14, different observations can be done :

- The curves respect the behaviour expected by the phenomenology of the dynamic stall : an increment of lift occurs after the static stall angle of attack is reached and the lift coefficient undergoes values lower than the static ones after the stall has occurred.
- The tangential force coefficient of the ALM in the downstream part of the rotor (i.e. when the angle of attack is negative) is indeed higher than the other ones.
- A kind of singularity is also visible for the three models on the drag force curve at an angle of attack approximately equal to 20°. This corresponds to the ejection of the dynamic stall vortex from the suction side of the blade and the tangential and normal forces therefore stall. However, as the tangential force coefficient plunges while the normal force one still stays for some time steps at relatively high values, the drag coefficient briefly goes up again after a small decrease.
- The tangential force coefficient is higher in the downstream part of the rotor than in the upstream part while it was the contrary for the tangential force curve : this is explained by the adimentionalization of the forces, taking into account the incident velocity on the blade, that has decayed in the downstream part.

4.3.2 Power coefficient

In this small subsection, the evolution of the power coefficient C_P is analyzed in function of the TSR for the different methods. Figure 4.15 shows that the ALM and the ACM provide more power than the VPM simulation for all the TSRs. The difference accentuates at high TSR but as the dynamic stall effects then disappear, only the low TSR are for interest in this work. The fact that the tangential force is higher for the ALM and the ACM than for the VPM method explains the higher power coefficient because the latter is based on the torque, itself based on the tangential force. The difference in terms of resolution of the mesh can justify the gap between ALM or ACM and VPM; the VPM simulations are done at a resolution of 48 mesh points per diameter while there are only 32 mesh points per diameter for ALM or ACM.

Stars are also put on figure 4.15 to indicate the power coefficients when the dynamic stall model is not taken into account at the three working TSRs. As expected, this nearly changes nothing for high TSRs but for the lower ones, it can be observed that the dynamic stall model involves significant gains in terms of power.

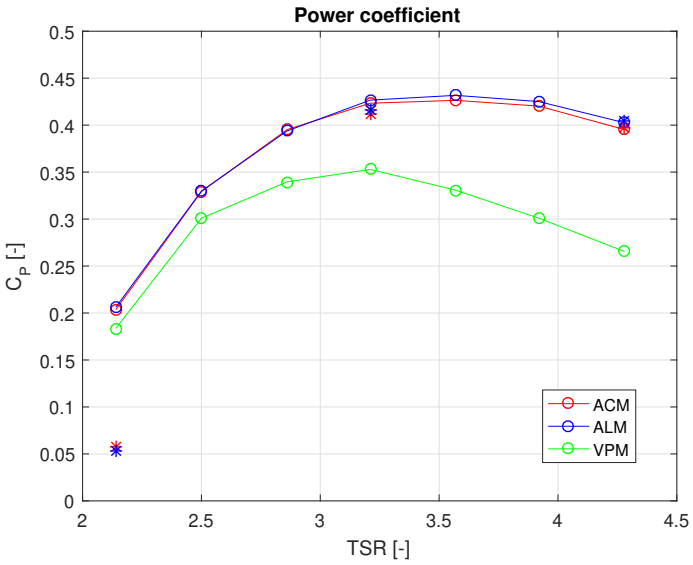

Figure 4.15: Power coefficient in function of the TSR

4.3.3 Wake analyses

The wakes of the ALM, ACM and VPM with dynamic stall and ALM and ACM without dynamic stall are compared for the three studied TSR through the adimensionalized mean streamwise velocity $\bar{u}/U_\infty$. Horizontal slices, taken at the mid-height of the wind turbine are shown on figures 4.16, 4.17 and 4.18. It should be noted that the references for the axis were established differently in the VPM simulations, i.e. the direction orthogonal to the VAWT axis being the y axis instead of the z axis.

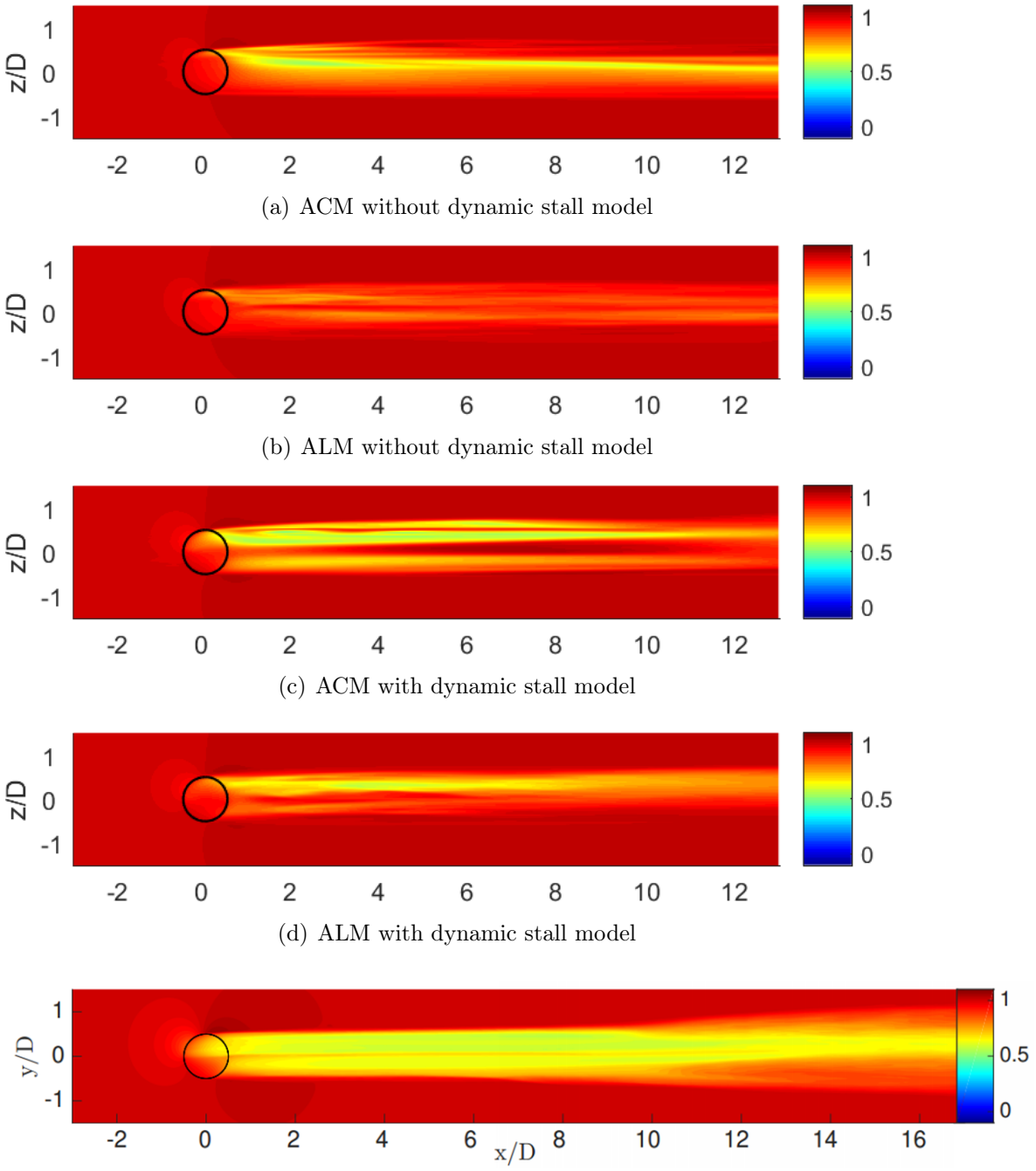

(a) ACM without dynamic stall model

(b) ALM without dynamic stall model

(c) ACM with dynamic stall model

(d) ALM with dynamic stall model

(e) VPM with dynamic stall model

Figure 4.16: Mean streamwise velocity $\bar{u}/U_\infty$ in the horizontal plane splitting the VAWT at mid-height for TSR 2.14

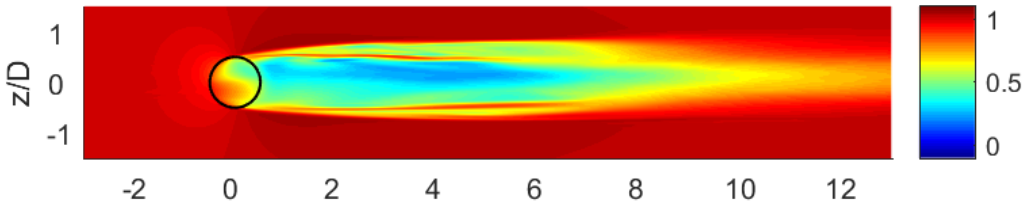

(a) ACM without dynamic stall model

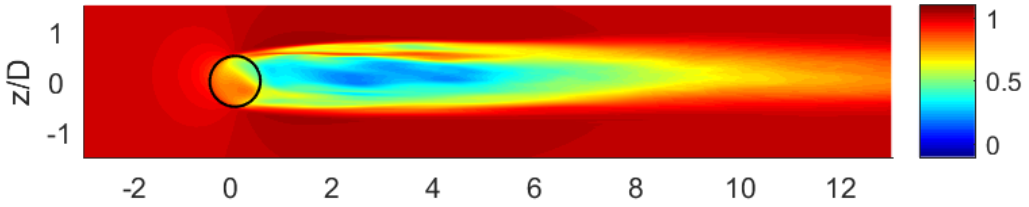

(b) ALM without dynamic stall model

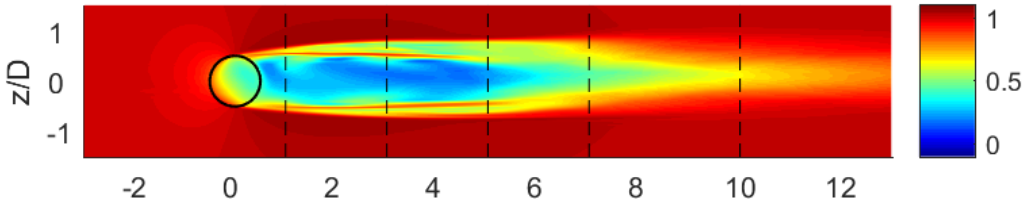

(c) ACM with dynamic stall model

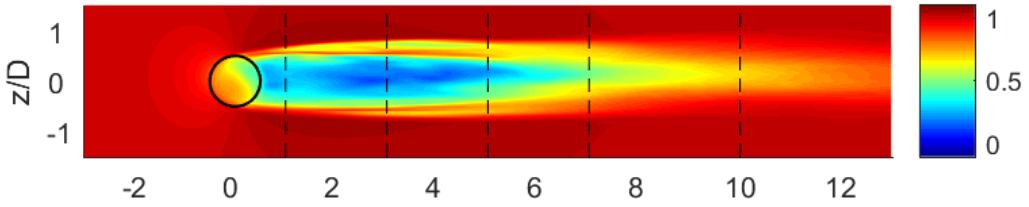

(d) ALM with dynamic stall model

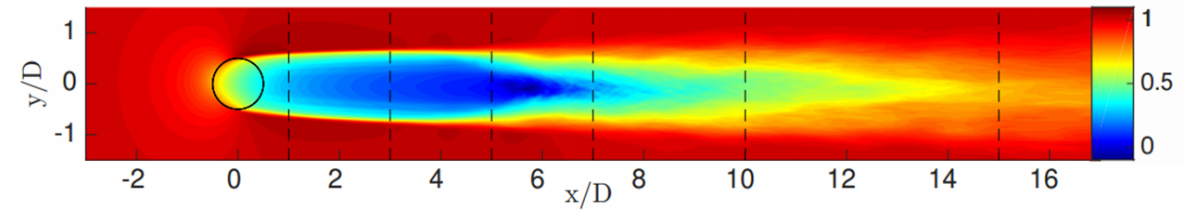

(e) VPM with dynamic stall model

Figure 4.17: Mean streamwise velocity $\bar{u}/U_\infty$ in the horizontal plane splitting the VAWT at mid-height for TSR 3.21

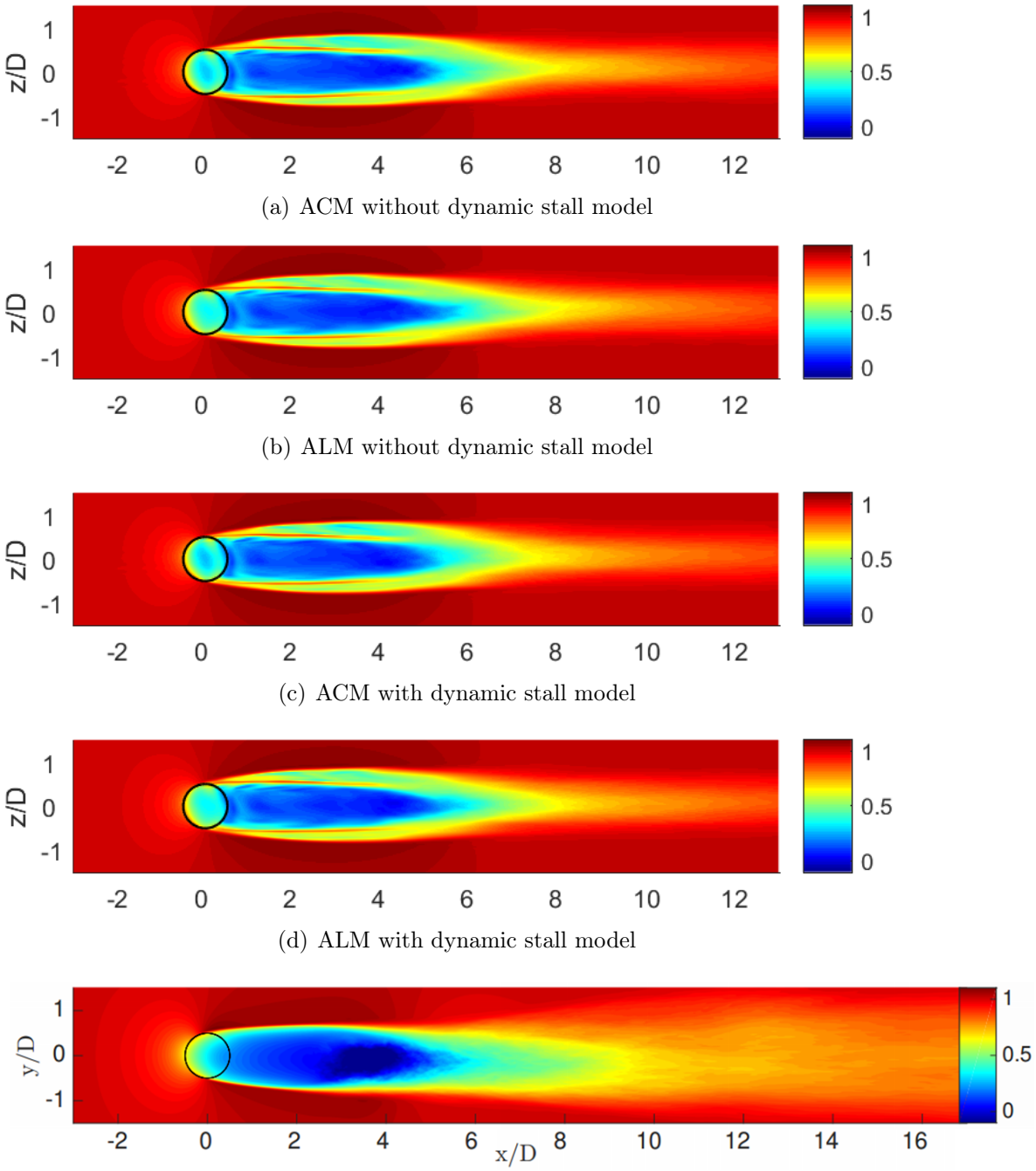

(a) ACM without dynamic stall model

(b) ALM without dynamic stall model

(c) ACM with dynamic stall model

(d) ALM with dynamic stall model

(e) VPM with dynamic stall model

Figure 4.18: Mean streamwise velocity $\bar{u}/U_\infty$ in the horizontal plane splitting the VAWT at mid-height for TSR 4.28

Comparing all these wakes leads to several observations. Firstly, the wake is governed by the TSR : a high TSR implies a shorter wake as well as more instabilities. Furthermore, it can also be seen that the VPM velocity deficits are always more pronounced than the ALM and ACM ones. Recirculation zones are observed in VPM simulations (at $x/D \approx 5.5$ for TSR 3.21 and $x/D \approx 4$ for TSR 4.28) and are absent in the actuator line and actuator cylinder models.

Then, even if their wakes are pretty similar, some differences arise between the ALM and ACM. The velocity deficit appears to be more realistic in the case of the ALM, especially inside the VAWT rotor. Differences inside the VAWT rotor are also especially observable for the TSR 3.21 and these differences probably lead to the differences observed in terms of forces in the downstream part of the rotor. These differences can be seen more clearly on the volume rendering of vorticities shown on figures 4.19 and 4.20. Indeed, it can be observed that the ALM provides a circular blade signature whereas the ACM cannot intrinsically model these effects.

Figure 4.19: Volume rendering of the vorticity magnitude in the wake of the ACM for TSR 2.14.

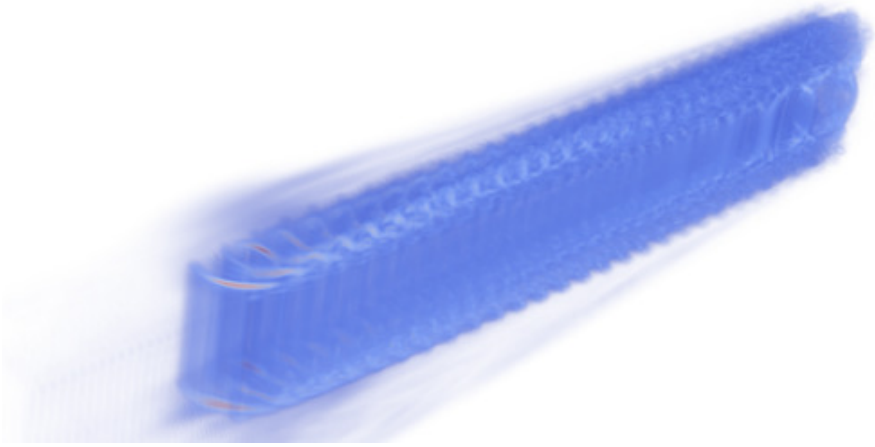

Figure 4.20: Volume rendering of the vorticity magnitude in the wake of the ALM for TSR 2.14.

Then, it might be worthy to compare wakes of ALM and ACM simulations with the dynamic stall model (figures 4.16(c), 4.16(d), 4.17(c), 4.17(d), 4.18(c) and 4.18(d)) to ALM and ACM simulations carried out without the dynamic stall model (figures 4.16(a), 4.16(b), 4.17(a), 4.17(b), 4.18(a) and 4.18(b)).

At the TSR 2.14, it can be observed that the velocity deficit is more important when the dynamic stall model is present for both the ALM and the ACM. This is not

surprising if it is considered that the dynamic stall model provides increments in terms of normal and tangential forces (see figure 4.3). The flow stalls with a delay with the dynamic stall and this is also logically reflected on the wakes. The wake is also more pronounced for the ACM than for the ALM but this is already the case in the static situation.

The delay of stall induced by the dynamic stall can of course be seen on TSR 2.14, but also on TSR 3.21 and especially for the ACM. Indeed, the velocity deficit inside the rotor is much more pronounced with the dynamic stall model and the two-lobed structure with a stronger deficit in the first half of the upstream part, that was visible without dynamic stall, disappears, which shows that the stall event has been delayed.

The wakes with and without the dynamic stall model for the TSR 4.28 are quite similar, which is expected as the dynamic stall effects disappear for high TSRs.

4.4 Improved model in uniform flow

In this section, the improved model of dynamic stall is analyzed taking the two following modifications into account : addition of two fictive separation points to better fit the tangential force data and modification of the C_n and C_t to account for the fact that C_t is sometimes negative (see section 2.3.4). The constants used are the ones derived in section 2.3.5 and coming from a NACA0015 polar at a Reynolds 680000. The results of the previous section show that the dynamic stall effects are not present at high TSRs thus only the TSR 2.14 is analyzed here. Furthermore, as the modifications to the dynamic stall model do not induce modifications in the wakes of the VAWT, they are not described here but can be found in appendix B. The numerical set-up is exactly the same as described in section 4.2.

The evolution of the angle of attack along one revolution is shown on figure 4.21, the forces are depicted on figure 4.22 and the force coefficients are outlined on figure 4.23. The curves for the improved model (solid) are always compared to curves representing the dynamic stall model that was used in the VPM simulations (dashed) at the Reynolds of 680000.

As expected, the evolution of the angle of attack does not change compared to the previous dynamic stall model and the normal force curve does not change either. By contrast, the tangential force is logically impacted by the modifications and the improved model proves to deliver more tangential force, whether it is in the upstream or downstream part of the rotor. These differences consistently reverberate in the tangential force coefficient. Whereas the normal and lift force coefficients do not seem to be affected, the improved model also provides less drag than the previous one. One can also remark that the differences observed earlier between ACM and ALM remain unchanged when adding this improved dynamic stall model.

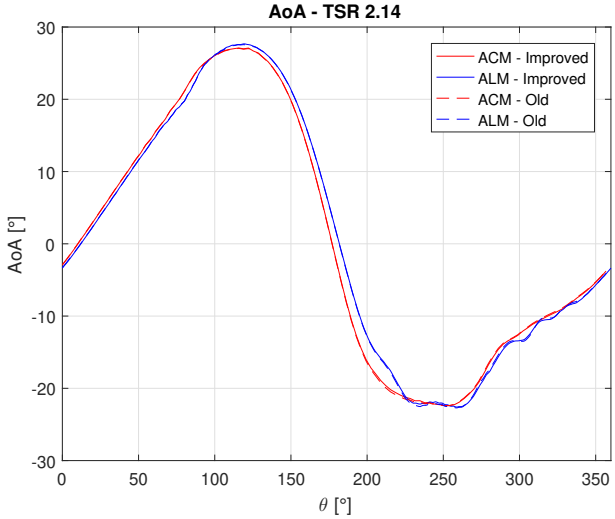

Figure 4.21: Angle of attack in function of the azimuthal position θ.

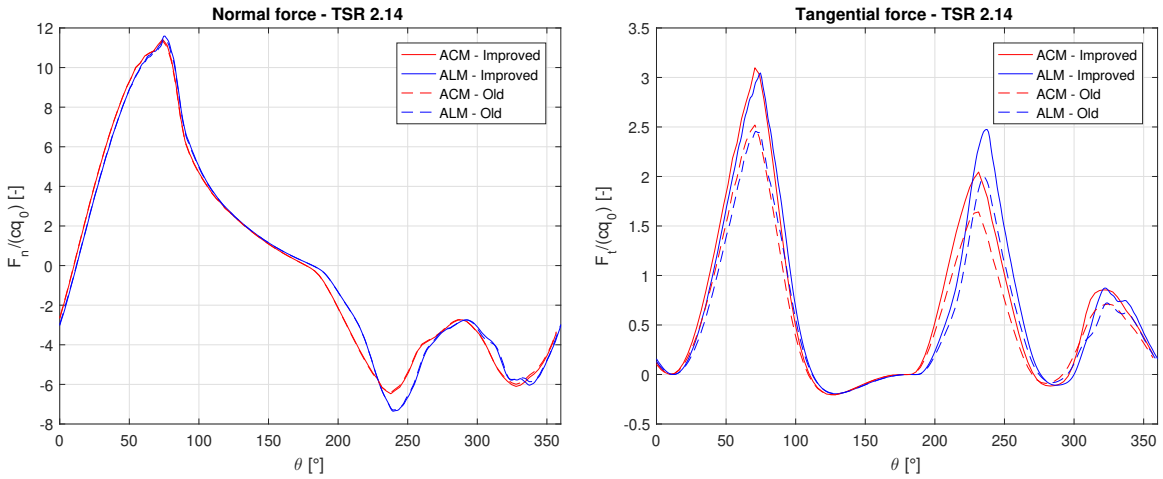

Figure 4.22: Normal and tangential forces in function of the azimuthal position θ for TSR 2.14

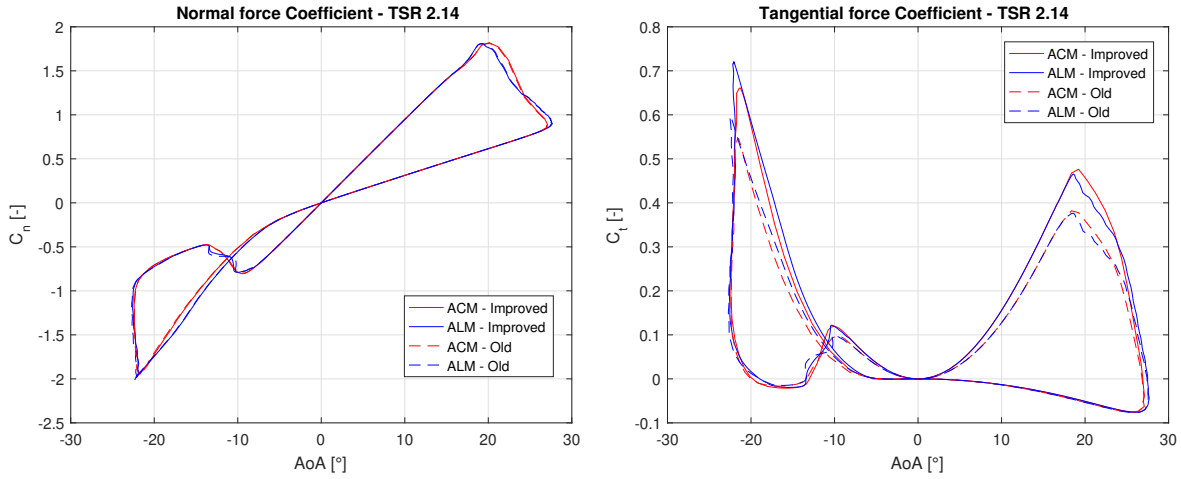

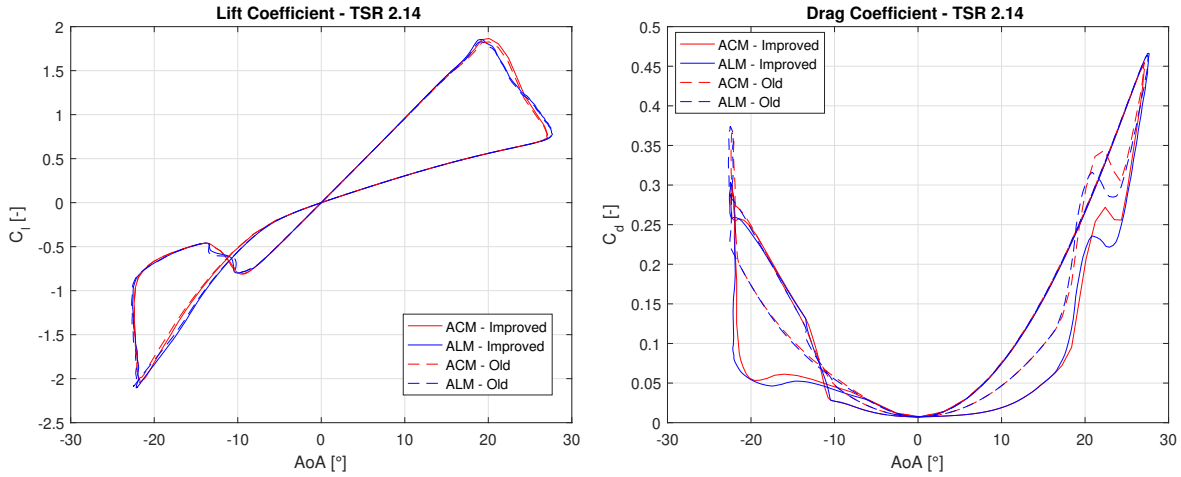

Figure 4.23: Normal, tangential, lift and drag force coefficients in function of the angle of attack for TSR 2.14

As the tangential force is responsible for the torque of the VAWT, using the improved model provides a significant increase in terms of power coefficient. The modifications done to better handle the dynamic stall by better fitting the static data of the tangential force coefficient thus demonstrate that the positive influence of the dynamic stall on the power coefficient was underestimated in the model of dynamic stall used in the VPM simulations. Table 4.3 summarizes the C_P for the TSR 2.14.

Model used	ACM - Improved	ALM - Improved	ACM - Old	ALM - Old
C_P [−]	0.2528	0.2536	0.2043	0.2058

Table 4.3: Power coefficients C_P in function of the model for the TSR 2.14

4.5 Improved model in turbulent flow

In this last section, the actuator line and actuator cylinder approaches with the improved model of dynamic stall are compared in a turbulent flow. Because the addition of turbulence by far rises the computational cost, the numerical set-up is slightly modified to reduce it. The simulations are now processed on a box with a size of $16D$x$8D$x$8D$ and the resolution of the mesh grid decreases from 32 points per diameter to 16 points per diameter in the streamwise and spanwise directions. This could lead to a small blockage effect as well as less accurate results (as demonstrated by the convergence analysis, see section 4.2) but as the comparisons are carried out between the ALM and the ACM with the same set-ups, they remain fair and reliable. The simulations are only done for the TSR 2.14 at a Reynolds number of 680000.

4.5.1 Turbulence model

The turbulence is generated using the Mann's algorithm (see [21] for more information). The global idea is to impose a pre-generated turbulent field over the mean inflow velocity [26]. The turbulence intensity (TI) [3], is of 7.5%, which corresponds to a low to medium level of turbulence. As a comparison, a TI of 5% relates to the average turbulence intensity encountered by offshore wind turbines [31].

4.5.2 Forces analysis

The evolution of the angle of attack is shown on figure 4.24, the normal and tangential forces on figure 4.25 and the aerodynamic coefficients on figure 4.26.

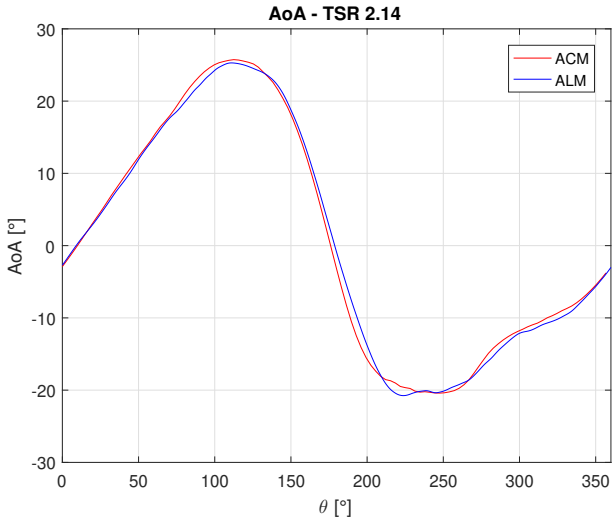

Figure 4.24: Angle of attack in function of the azimuthal position θ, turbulent flow.

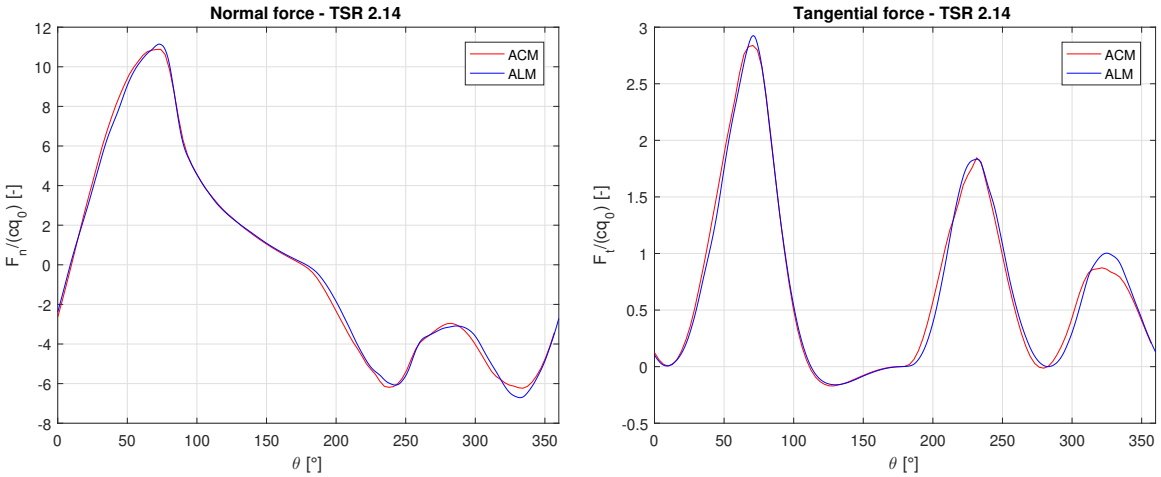

Figure 4.25: Normal and tangential forces in function of the azimuthal position θ for TSR 2.14, turbulent flow.

[3] $TI = \frac{u'}{U}$ with $u' = \sqrt{\frac{1}{3}(u'^2 + v'^2 + w'^2)}$ and $U = \sqrt{(\bar{u}^2 + \bar{v}^2 + \bar{w}^2)}$

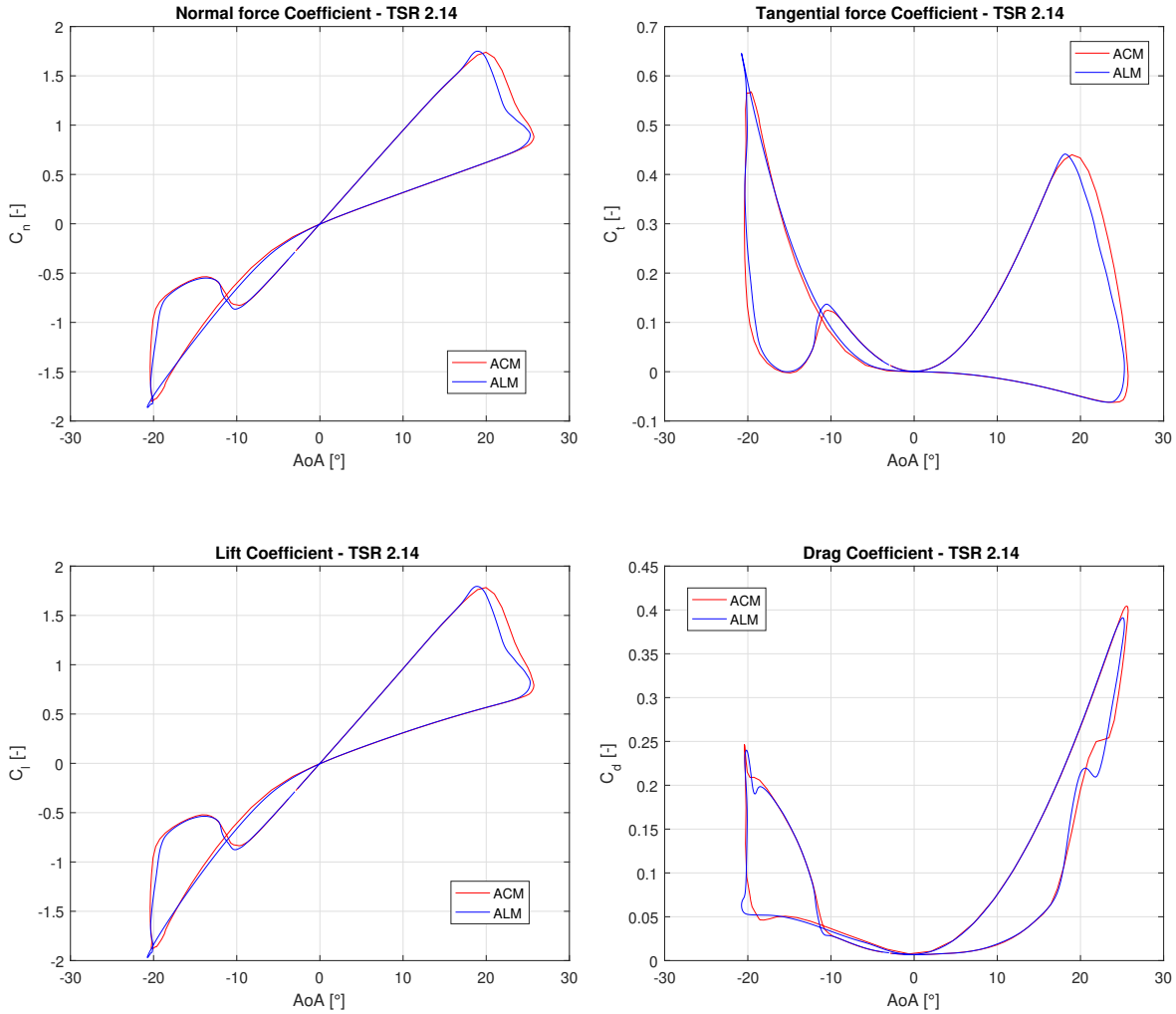

Figure 4.26: Normal, tangential, lift and drag force coefficients in function of the angle of attack for TSR 2.14, turbulent flow.

Firstly, it can be seen that the general behaviour of the curves follows the uniform flow one, meaning that the dynamic stall model behaves well even if the blades encounter variations of angle of attack due to the turbulence and no longer only due to their rotational movement.

Secondly, it can be observed in these graphs that the turbulence tends to bring the ALM and ACM closer. This phenomenon is especially visible on the downstream part of the tangential force related graphs, where the ALM used to produce more tangential force than the ACM in uniform flow. This is explained by the wake analysis (see following section 4.5.3) : as the velocity fields are not only due to the wakes of the wind turbines anymore but also to the ambient turbulence, the velocity deficits tend to be more similar between ALM and ACM. Indeed, the ambient turbulence further impacts the flow inside the area swept by the VAWT, reducing the differences between ALM and ACM. Especially the important differences seen inside the rotor in uniform flow are smoothed and so are the differences in terms of tangential forces in the downstream part of the rotor. Thus, the differences in terms of power coefficient are also reduced between the actuator cylinder and the actuator line models.

4.5.3 Wakes analyses

The wakes are shown on figure 4.27. The first figures present snapshots of the adimensionalized streamwise velocity u/U_∞ after 3 convective times, the second figures describe the adimensionalized mean streamwise velocity $\bar{u}/U_\infty$ and the third figures represent the turbulent kinetic energy $\bar{k}$ (TKE) [4].

As explained just before, the velocity deficits tend to get closer thanks to the turbulence. The circular blade signatures characteristic to the wake of the ALM (see figure A.1 of appendix A for the instantaneous wakes in uniform flows) are still visible in the snapshot but are by far attenuated compared to the ones in uniform flow. Also, the kind of lines that emerged from the boundaries of the VAWT (azimuthal positions θ = 0° and 180°) disappear because of the ambient turbulence. The TKE is relatively similar between the two methods, except that almost no TKE is produced inside the rotor for the ACM. One can also observe that there is no production of TKE due to the dynamic stall vortices that are ejected from the blades. This makes sense as the ALM and the ACM modulate the forces in function of the dynamic stall phenomenon, but no mechanism is present to represent the shed vortices. As the TSR is not especially high, few TKE is generated.

Next, cross-flow slices of the mean streamwise velocity and TKE at different x/D positions starting from the center of the VAWT are depicted on figures 4.28 and 4.29. One difference arises in the fact that small lobes are observable just above and below the VAWT after one adimensional position in the ACM and not in the ALM. This behaviour could be explained by the forces distribution kernels that differ between the two methods : a 3D kernel is used in the ACM while a 2D kernel is used in the ALM. Therefore, no forces are distributed past the tips of the blades in the latter. Otherwise, the general behaviour of the mean streamwise velocity and TKE are globally similar on these cross-flow slices, the structures of the wakes decay to provide turbulent and random velocity fields.

[4] $\bar{k} = \frac{\overline{u'u'}+\overline{v'v'}+\overline{w'w'}}{2U_\infty^2}$

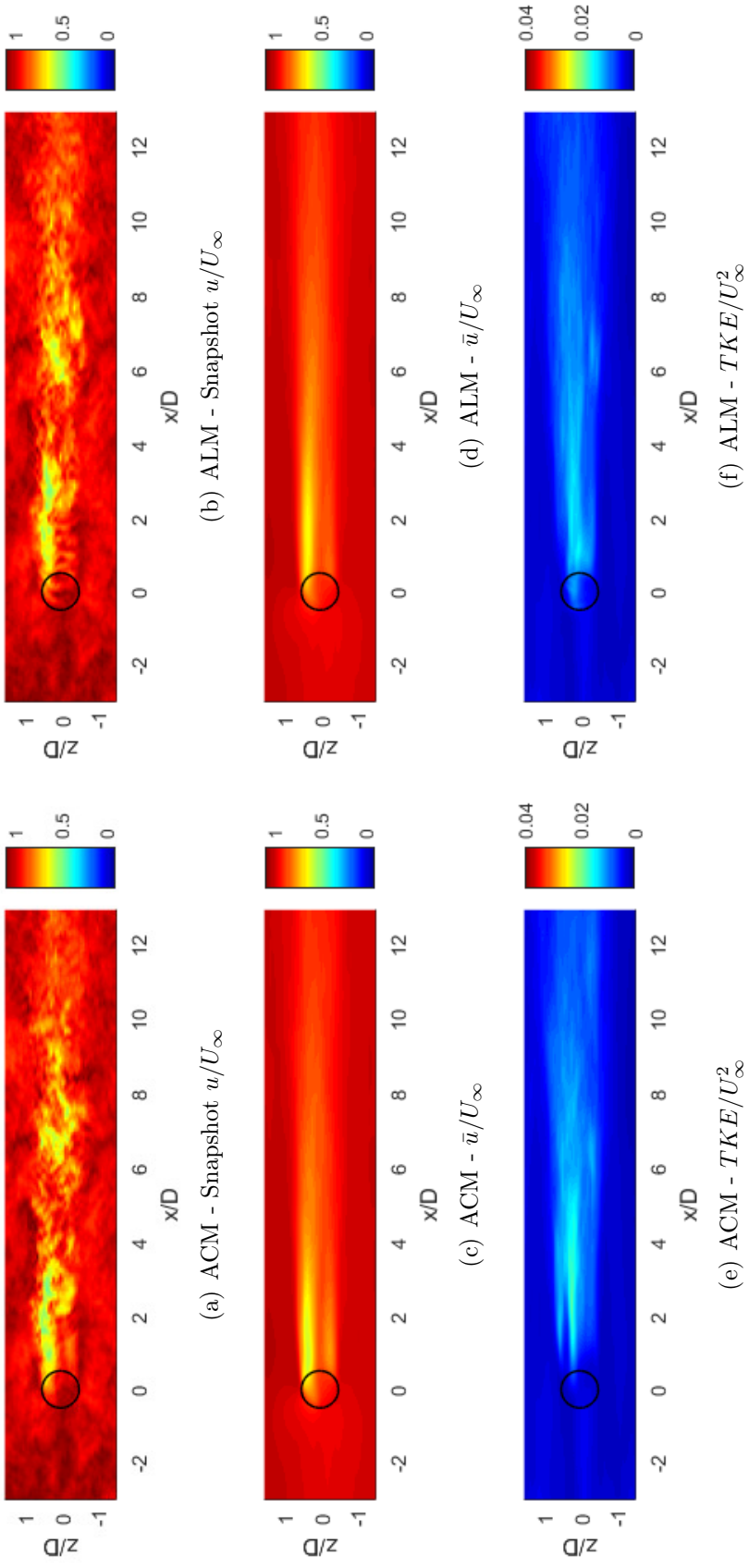

(a) ACM - Snapshot u/U_∞ (b) ALM - Snapshot u/U_∞

(c) ACM - $\bar{u}/U_\infty$ (d) ALM - $\bar{u}/U_\infty$

(e) ACM - TKE/U_∞^2 (f) ALM - TKE/U_∞^2

Figure 4.27: Wakes in turbulent flow

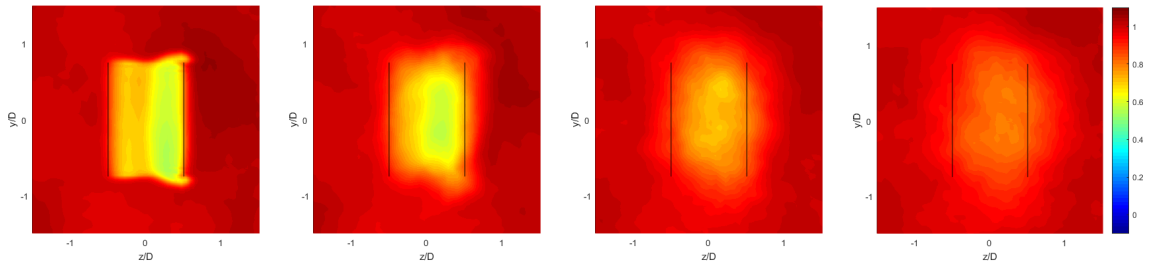

(a) x/D = 1 (b) x/D = 4 (c) x/D = 7 (d) x/D = 10

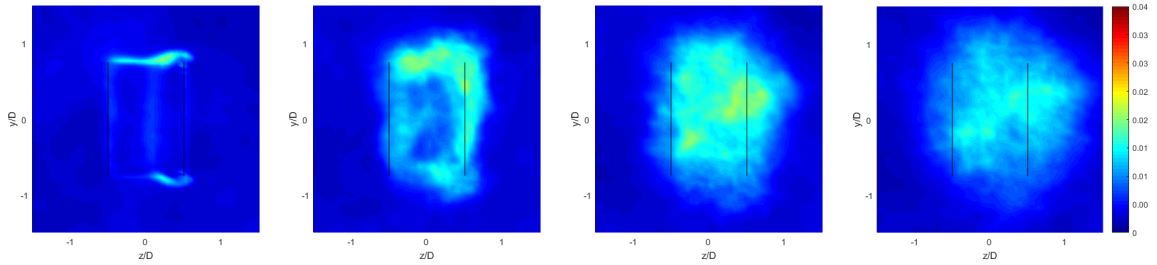

(e) x/D = 1 (f) x/D = 4 (g) x/D = 7 (h) x/D = 10

Figure 4.28: Cross-flow slices ACM in turbulent flow - Above : $\bar{u}/U_\infty$, Below : TKE/U_∞^2

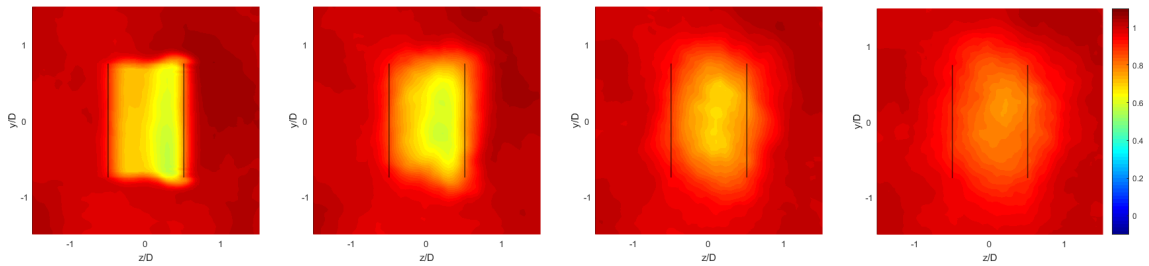

(a) x/D = 1 (b) x/D = 4 (c) x/D = 7 (d) x/D = 10

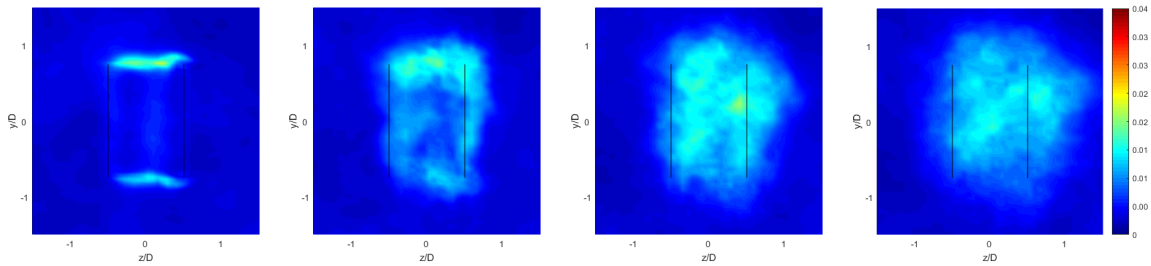

(e) x/D = 1 (f) x/D = 4 (g) x/D = 7 (h) x/D = 10

Figure 4.29: Cross-flow slices ALM in turbulent flow - Above : $\bar{u}/U_\infty$, Below : TKE/U_∞^2

Chapter 5

Conclusion and outlooks

This thesis was undertaken to analyze the complex phenomenon of dynamic stall in an actuator line and surface models for the context of vertical axis wind turbines.

The first part of this work focused on the theoretical investigation of the dynamic stall. After a description of the phenomenology and a review of the existing models, the choice was taken to go for the Leishman-Beddoes solutions to model the dynamic stall. These models were then detailed mathematically and even refined, gathering the input and ideas of other contributions.

The second part of the thesis was centred around the practical insertion of the chosen model of dynamic stall in existing codes of actuator line and actuator cylinder methods. The LB model was implemented respecting the specificities of each method of simulation of the VAWT.

The last part of this thesis presents the results of the implementation of the dynamic stall. The model was first validated thanks to the high-fidelity VPM simulation and a numerical set-up arose from a trade-off between a convergence analysis and the computational cost. Different simulations were carried out afterwards. Firstly, transverse simulations were done with the model of dynamic stall implemented in VPM to compare the ALM, ACM, VPM and DMST models for various TSRs. The ALM and ACM show good agreement between each other even if the ALM provides a higher peak of tangential force in the downstream part of the rotor and if some differences are visible in the velocity fields. The dynamic stall model was shown to induce a power increment with respect to the static case. Secondly, the improved model of dynamic stall taking into account two fictive separation points and modified normal and tangential force coefficients was investigated in an uniform flow and proved to provide more power than the previous model of dynamic stall. Thirdly, this improved model of dynamic stall was tested in a turbulent flow and one-to-one comparisons between ALM and ACM were performed. The latter taught that the two different models tend to get closer in terms of wakes and forces in a turbulent flow, to reach pretty similar results.

Further works could still be performed in order to improve the understanding of the dynamic stall in the context of VAWTs. Among other, it could be interesting to evaluate the effects of dynamic stall in wind farms of wind turbines at low TSRs. As the velocity deficit was shown to be more important when the dynamic stall model is present, the gain in terms of power thanks to the addition of this model could maybe

disappear for the VAWTs placed in the wake of another VAWT in comparison with the static case. Furthermore, an active pitch control could be designed to enhance the performance of the VAWTs. At last, one other idea could be to optimize the topology of the VAWT. Different possible geometries were presented in a non-exhaustive way in the introduction, but as only the H-VAWT was studied here, it could be worthy to do numerical comparisons and optimisations to find the most efficient geometry.

Bibliography

[1] Bachant P., Goude A., Wosnik M., *Actuator line modeling of vertical-axis turbines*, University of New Hampshire, USA, 2018.

[2] Balbino R., *Validating the Beddoes-Leishman Dynamic Stall Model in the Horizontal Axis Wind Turbine Environment*, Master Thesis on Aerospace Engineering, Universidade Técnica de Lisboa, Instituto superior técnico, 2010.

[3] Bangga G., Dessoky A., Lutz T., Krämer E., *Improved double-multiple-streamtube approach for H-Darrieus vertical axis wind turbine computations*, Institute of Aerodynamics and Gas Dynamics (IAG), University of Stuttgart, Germany, 2019.

[4] Beddoes T.S., *Representation of airfoil behaviour*, Vertica, Vol 7, No. 2, pp. 183-197, 1983.

[5] Chantharasenawong C., *Nonlinear Aeroelastic Behaviour of Aerofoils Under Dynamic Stall*, PhD Thesis, Department of Aeronautics, Imperial College London, South Kensington Campus, 2007.

[6] Beaudet L., *Etude expérimentale et numérique du décrochage dynamique sur une éolienne à axe vertical de forte solidité*, Phd thesis, Université de Poitiers, Ecole Doctorale Sciences et Ingénierie en Matériaux, Mécanique, Energétique et Aéronautique, Poitiers, 2014.

[7] Chatelain P., Duponcheel M., Caprace D-G., Marichal Y., Winckelmans G., *Vortex Particle-Mesh simulations of Vertical Axis Wind Turbine flows : from the blade aerodynamics to the very far wake*, European academy of wind energy, 2017.

[8] Cheng Z., Madsen H.A., Gao Z., Moan T., *Aerodynamic modeling of floating vertical axis wind turbines using the actuator cylinder flow method*, Energy procedia, 94:531-543, 2016.

[9] Collin C., Moëns V., *Numerical investigation of an offshore vertical axis wind turbine farm : from the wind resource to the control and power generation*, Master thesis, Ecole Polytechnique de Louvain, UCLouvain, 2017.

[10] Cooper P., *Development and analysis of vertical-axis wind turbines*, Wind Power Generation and Wind Turbine Design - Chapter 8, 2010.

[11] Donnay M., Lallemand Q., *Conception d'un aérogénérateur à axe vertical fabricable par des techniques de prototypage rapide*, Master thesis, Ecole Polytechnique de Louvain, UCLouvain, 2016.

[12] Duponcheel M., *Direct and large-eddy simulation of turbulent wall-bounded flows : further development of a parallel solver, improvement of multiscale subgrid models and investigation of vortex pairs in ground effect*, Phd thesis, Ecole Polytechnique de Louvain, UCLouvain, 2009.

[13] Dyachuk E., Goude A., Bernhoff H., *Dynamic Stall Modelling for the Conditions of Vertical Axis Wind Turbines*, Uppsala University AIAA JOURNAL Vol. 52, No. 1, 2014.

[14] Elia, *Press release,* Brussels, 2018.

[15] Fraunhofer institute for solar energy systems, *Levelized cost of electricity, renewable energy technologies*, Freiburg, March 2018.

[16] Houf D.P., *Active Pitch Control of a Vertical Axis Wind Turbine*, Master thesis, TU Delft, 2016.

[17] Larsen J.W., Nielsen S.R.K., Krenk S., *Dynamic stall model for wind turbine airfoils*, Journal of Fluids and Structures, vol. 23, no. 7, pp. 959–982, 2007.

[18] Lee M., Oh B., Kim Y., *Canonical fractional-step methods and consistent boundary conditions for the incompressible Navier-Stokes equations*, Journal of computational physics, 2001.

[19] Leishman J.G., *Principles of Helicopter Aerodynamics*, 2nd Edition, Cambridge University Press, 2006.

[20] Madsen H.A., *The actuator cylinder - a flow model for vertical axis wind turbines*, Aalborg University, 1982.

[21] Mann J., *Wind field simulation*, Probabilistic Engineering Mechanics, 13(4):269 – 282, 1998.

[22] Marchesse Y., *Modélisation de la turbulence*, Ecole Catholique d'Arts et Métiers de Lyon, 2010.

[23] Marichal Y., Caprace D-G., Chatelain P., *Leishman-Beddoes dynamic stall model inside VIC-Eole/VPM4x*, Ecole Polytechnique de Louvain, UCLouvain, 2016.

[24] Mendoza V., Bachant P., Ferreira C., Goude A., *Near-wake flow simulation of a vertical axis turbine using an actuator line model*, Wind Energy;22:171–188, 2019.

[25] Moens M., Duponcheel M., Winckelmans G., Chatelain P., *Les of wind farm response to transient scenarios using a high fidelity actuator disk model*, Journal of Physics: Conference Series, 753, 2016.

[26] Moens M., *Large eddy simulation of wind farm flows : improved Actuator Disk model and investigations of wake phenomena*, PhD Thesis, Ecole Polytechnique de Louvain, UCLouvain, 2018.

[27] Moghimi M., Motawej H., *Developed DMST model for performance analysis and parametric evaluation of Gorlov vertical axis wind turbines*, School of mechanical engineering, Iran University of Science & Technology, Tehran, 2019.

[28] Monaghan J.J., *Extrapolating b splines for interpolation*, Journal of Computational Physics, 60:253-262, 1985.

[29] Sheldahl R.E., Klimas P.C., *Aerodynamic characteristics of seven symmetrical airfoil sections through 180-degree angle of attack for use in aerodynamic analysis of vertical axis wind turbines*, No. SAND-80-2114. Sandia National Labs., Albuquerque, NM(USA), 1981.

[30] Scheurich F., *Modelling the aerodynamics of vertical-axis wind turbines*, PhD Thesis, University of Glasgow, 2011.

[31] Siddiquia M.S., Rasheed A., Kvamsdal T., Tabib M., *Effect of Turbulence Intensity on the Performance of an Offshore Vertical Axis Wind Turbine*, 12th Deep Sea Offshore Wind R&D Conference, EERA DeepWind'2015.

[32] Sørensen J.N., Shen W.Z., *Numerical modeling of wind turbine wakes*, Journal of Fluids Engineering, 2002.

[33] Taverne Q., *Modélisation par forces surfaciques d'éoliennes à axe vertical*, Master thesis, Ecole Polytechnique de Louvain, UCLouvain, 2015.

[34] Trigaux F., *Actuator lines modeling and investigation of tilted wind turbines for improved farm efficiency*, Master thesis, Ecole Polytechnique de Louvain, UCLouvain, 2019.

[35] Urbina R., Peterson M.L., Kimball R.W., Debree G.S., Kimball M.P., *Modelling and validation of a cross flow turbine using free vortex model and a modified dynamic stall model*, Renewable Energy 50, 662–669, 2013.

[36] Walther J.H., Koumoutsakos P., *Three-dimensional vortex methods for particle laden flows with two-way coupling*, Journal of Computational Physics, 167:39-71, 2001.

[37] Waltzing J. *Development of an actuator surface method for vertical axis wind turbines*, Master thesis, Ecole Polytechnique de Louvain, UCLouvain, 2020.

[38] WaPT, Wake Prediction Technologies, https://www.wapt.be/

[39] Winckelmans G., Bricteux L., *Numerical methods in fluid mechanics*, Ecole Polytechnique de Louvain, UCLouvain, 2020.

[40] World Energy Council, *World Energy Scenarios*, 2019.

Appendices

Appendix A

Instantaneous wakes with VPM constants

The instantaneous visualizations of the adimensionalized streamwise velocity are shown on figure A.1. They refer to part 4.3, in which the dynamic stall with the VPM constants is discussed.

These snapshots are interesting to clearly see the differences between a discrete blade approach and an averaged blade approach. Vorticity structures due to the blades can be seen on the actuator line simulations which is not the case on the actuator cylinder ones.

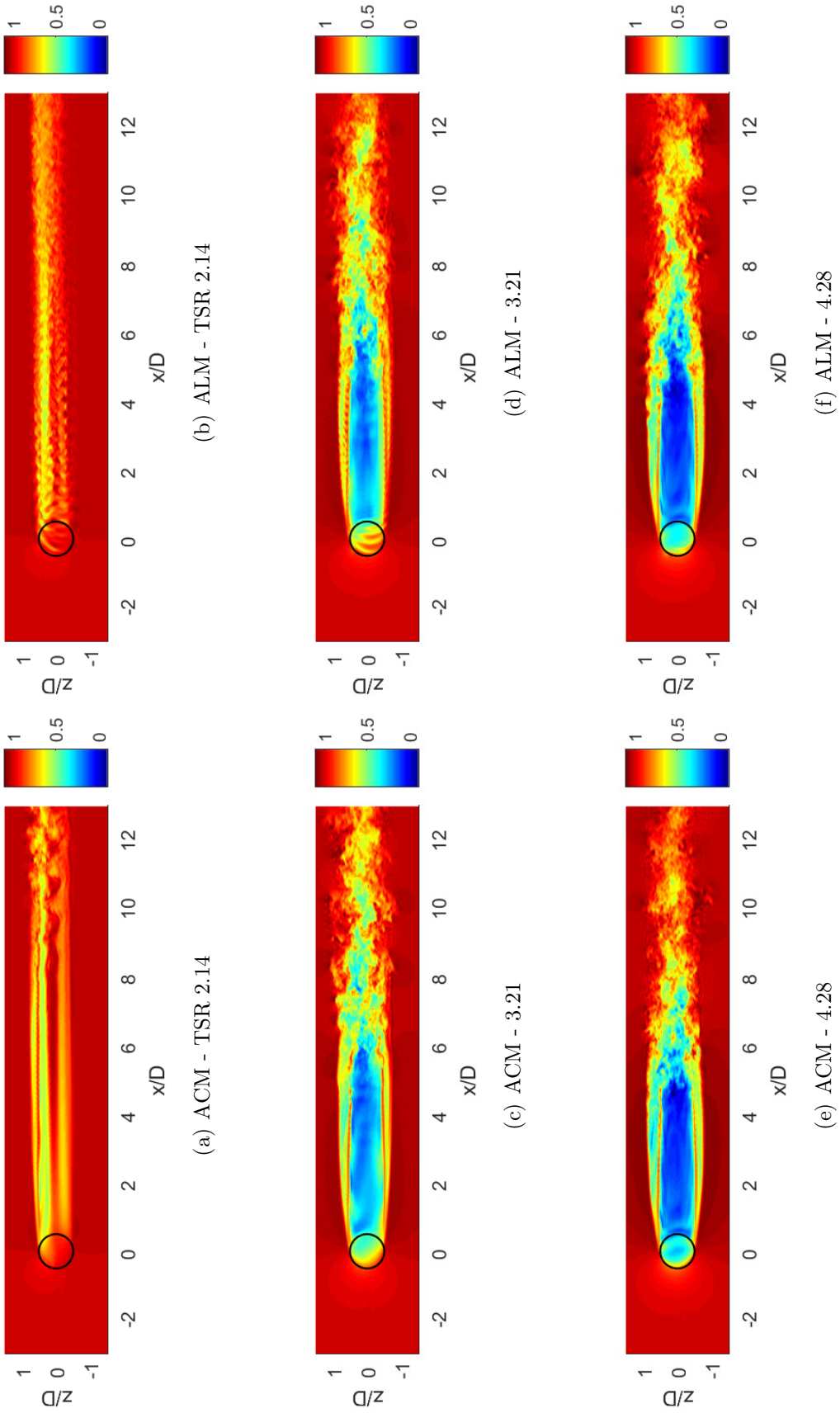

(a) ACM - TSR 2.14 (b) ALM - TSR 2.14

(c) ACM - 3.21 (d) ALM - 3.21

(e) ACM - 4.28 (f) ALM - 4.28

Figure A.1: Instantaneous wakes in uniform flow, u/U_∞

Appendix B

Mean wake of the improved model for TSR 2.14

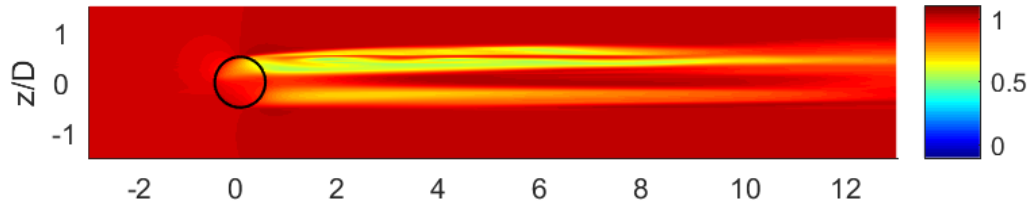

(a) ACM

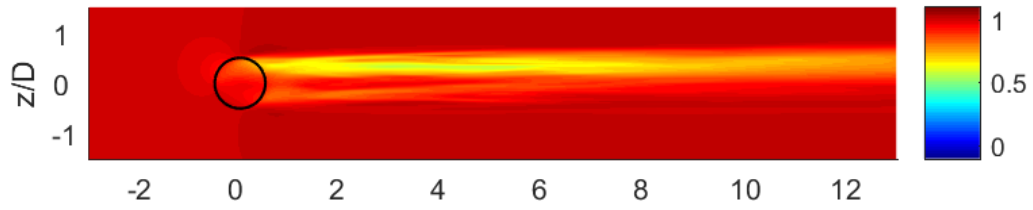

(b) ALM

Figure B.1: Mean streamwise velocity $\bar{u}/U_\infty$ in the horizontal plane splitting the VAWT at mid-height for TSR 2.14

UNIVERSITÉ CATHOLIQUE DE LOUVAIN
École polytechnique de Louvain
Rue Archimède, 1 bte L6.11.01, 1348 Louvain-la-Neuve, Belgique | **www.uclouvain.be/epl**